# Block modeling of crustal deformation of the northern Walker Lane and Basin and Range from GPS velocities

William C. Hammond,[1] Geoffrey Blewitt,[1] and Corné Kreemer[1]

Received 29 June 2010; revised 19 January 2011; accepted 24 January 2011; published 7 April 2011.

[1] We infer rates of crustal deformation in the northern Walker Lane (NWL) and western Basin and Range using data from the Mobile Array of GPS for Nevada transtension, and other continuous GPS networks including the EarthScope Plate Boundary Observatory. We present 224 new GPS velocities, correct them for the effects of viscoelastic postseismic relaxation, and use them to constrain a block model to estimate fault slip rates. The data segregate the NWL into domains based on differences in deformation rate, pattern, and style. Deformation is transtensional, with highest rates near the western and eastern edges of the NWL. Some basins, e.g., Tahoe, experience shear deformation and extension. Normal slip is distributed throughout the NWL and Basin and Range, where 11 subparallel range-bounding normal fault systems have an average horizontal extension rate of 0.1 mm/yr. Comparison between geologic and geodetic slip rates indicates that out of 12 published geologic rates, 10 agree with geodetic rates to within uncertainties. This suggests that smaller crustal blocks move steadily, similar to larger lithospheric plates, and that geodetic measurements of slip rates are reliable in zones of complex crustal deformation. For the two slip rates that disagree, geologic rates are greater. The vertical axis rotation rate of the Carson domain is $-1.3 \pm 0.1$°/My clockwise, lower than the 3° to 6°/My obtained in paleomagnetic measurements. This suggests that vertical axis rotation rates may have decreased over the last 9–13 My as the role of faulting has increased at the expense of rigid rotations.

**Citation:** Hammond, W. C., G. Blewitt, and C. Kreemer (2011), Block modeling of crustal deformation of the northern Walker Lane and Basin and Range from GPS velocities, *J. Geophys. Res.*, *116*, B04402, doi:10.1029/2010JB007817.

## 1. Introduction

[2] The northern Walker Lane (NWL) is a structurally complex zone of transition between the Sierra Nevada/Great Valley microplate (SNGV) and the Basin and Range Province of the western United States (Figure 1). Evidence from seismic [e.g., *Ichinose et al.*, 2003; *Unruh et al.*, 2003], geodetic [e.g., *Argus and Gordon*, 1991; *Thatcher et al.*, 1999; *Bennett et al.*, 2003; *Svarc et al.*, 2002; *Oldow*, 2003; *Hammond and Thatcher*, 2004], and geologic studies [e.g., *Dokka and Travis*, 1990; *Wesnousky*, 2005a] together indicate that this ~100 km wide zone is actively deforming and accommodates ~20% of the relative motion between the Pacific and North American tectonic plates.

[3] In 2004 the Mobile Array of GPS for Nevada Transtension (MAGNET) was deployed to study NWL deformation patterns, resolve strain rates, and estimate slip rates on crustal block-bounding faults. MAGNET is a complement to the EarthScope Plate Boundary Observatory (PBO) which includes ~1100 high-precision permanent stations in the western United States. In MAGNET the crustal velocity field is sampled using a semicontinuous methodology [*Blewitt et al.*, 2009] that offers a compromise between geographically dense tripod-based campaign measurements [e.g., *Thatcher et al.*, 1999] and sparse but more precise continuous recording on deeply anchored permanent monuments [e.g., *Wernicke et al.*, 2000]. The semicontinuous method offers improved efficiency with respect to the precision and number of crustal motion rates obtainable under fixed cost.

[4] Here we use geodetic and geologic measures of crustal deformation to develop models of block motions and slip rates. Neotectonic and paleoseismic studies of seismic moment release rates are complementary to geodetic studies. Both methods measure the crustal deformation field, but over different times in the seismic cycle. Geologic and geodetic measures of deformation have been shown to be in good agreement across the scale of major plates and across many important plate boundary faults [*Thatcher*, 2009] (with some anomalies [e.g., *DeMets et al.*, 1994; *Wallace et al.*, 2004]). How well this agreement extends into smaller zones of distributed and complex deformation, on regional to individual fault scales, such as inside the NWL, has not been extensively studied. Close agreements between geologic and geodetic estimates of fault slip rates would suggest that

[1]Nevada Geodetic Laboratory, Nevada Bureau of Mines and Geology and Nevada Seismological Laboratory, University of Nevada, Reno, Nevada, USA.


0148-0227/11/2010JB007817

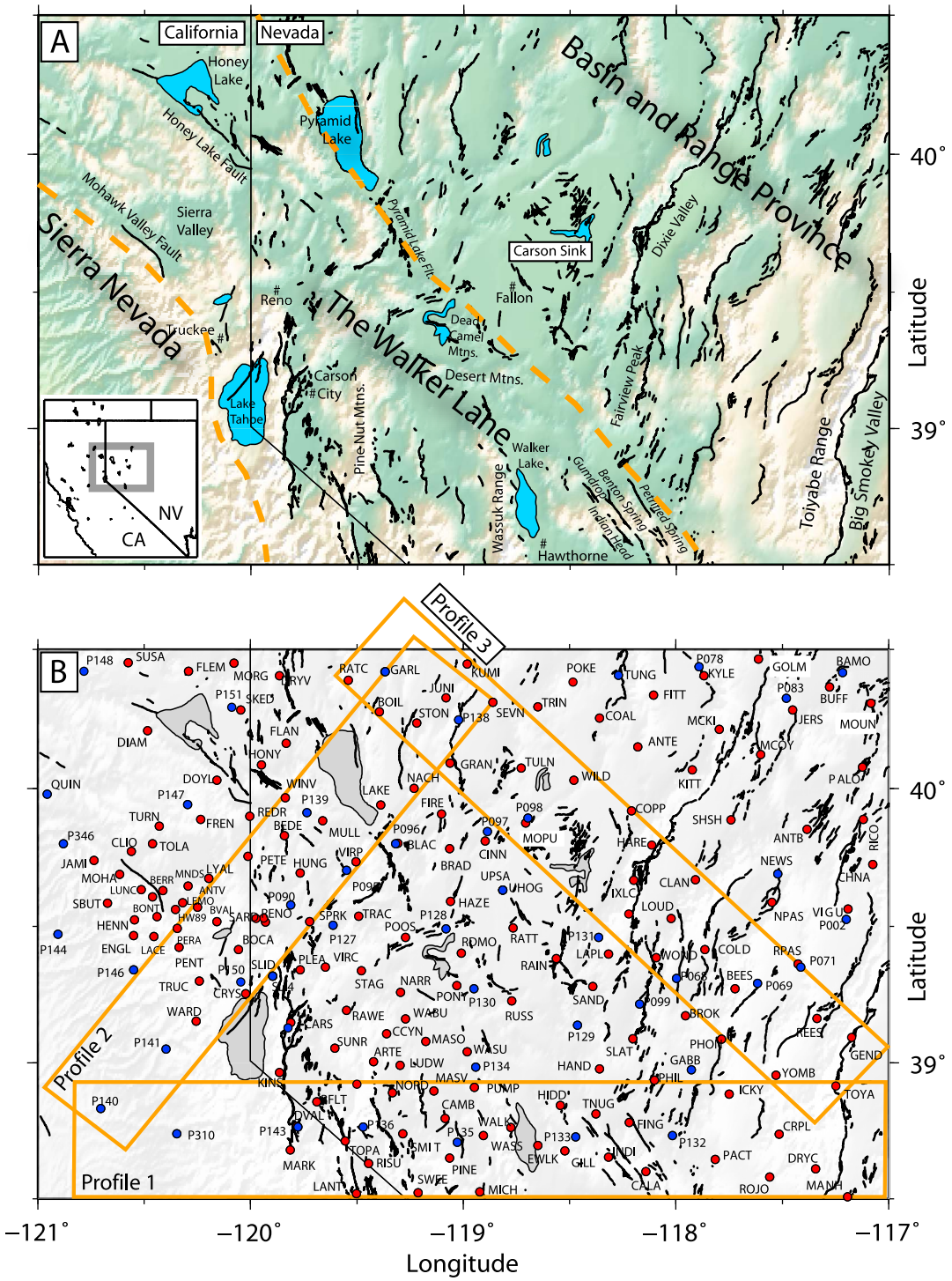


**Figure 1.** Northern Walker Lane region shaded topography and faults (black lines). (a) Place names on topography and faults, whose names are given in italics. East and west limits of Walker Lane are indicated with orange dashed line. Small inset shows location of region at the boundary between California and Nevada. (b) GPS site names are given next to MAGNET (red circles) and continuous GPS sites (blue circles). Orange outlines are locations of velocity profiles shown in Figure 3.

(1) patterns and rates of strain accumulation (measured geodetically) match patterns of strain release (measured in fault studies), (2) geodynamic processes responsible for observed faulting are presently active and measurable, and (3) that geodetic measurements can provide constraint on the likelihood for future earthquakes, and hence are an important tool for studies of seismic hazard.

[5] Relating GPS velocities made in the interseismic time to longer-term motions of blocks and slip rates on faults requires a modeling strategy that accounts for the fact that

faults are locked at the surface, but slip steadily and continuously at depth. We use a block modeling technique, similar to those used in other recently published analyses, that incorporates shallow locking of the faults and solves for fault slip rates and block rotations from GPS velocities [e.g., *McCaffrey*, 2002; *Meade and Hager*, 2005]. However, direct comparison between patterns of strain accumulation and release are made more complicated by transient seismic cycle effects that can distort the contemporary deformation field [*Pollitz et al.*, 2008]. In at least some cases disagreements between geologic and geodetic measurements can be attributed to the presence of viscoelastic relaxation following large earthquakes [e.g., *Segall*, 2002; *Dixon et al.*, 2003]. In particular the NWL GPS measurements are likely affected by viscoelastic relaxation following the Central Nevada Seismic Belt (CNSB) earthquakes [*Hetland and Hager*, 2003; *Gourmelen and Amelung*, 2005; *Hammond et al.*, 2009]. We correct the GPS data by removing transient viscoelastic relaxation effects, and subsequently infer the long-term secular motion of blocks.

## 2. GPS Data

### 2.1. MAGNET GPS Network

[6] The efficiency of MAGNET relies on several important features to achieve precision in rates of crustal motion that approach those obtained from continuous sites, but at a larger number of sites per unit cost. These are (1) fixed steel monument pins placed in stable bedrock or equivalent, to which a GPS antenna can be attached with precise repeatability, (2) a homogeneous pool of GPS receivers and antennas that minimizes biases associated with changes in GPS equipment, (3) a relatively large pool of GPS receivers that can be circulated through the network and occupy each site a significant fraction of each year, (4) a network that is near our workplace so that receivers can be moved from site to site throughout most of the year, and (5) equipment that can run in the field independently using solar power and data logging for months at a time between pickups [*Blewitt et al.*, 2009]. The number of sites and receivers employed in the network evolved over the course of the experiment, but as of this writing MAGNET consists of 307 sites surveyed by 57 Trimble 5700 and R7 dual frequency GPS receivers with Zephyr Geodetic antennas. The first site was first occupied in January 2004.

[7] We also use GPS observations from PBO and other continuous networks, some of which have been running for over 10 years, and from 6 continuous sites on the Sierra Nevada/Great Valley microplate (SNGV) that constrain its motion and verify its rigidity along the western boundary of the WL (sites CHO1, ORVB, P140, P276, P130, SUTB). Other sites around North America (NA) and the Great Basin were used to define the reference frame, as described below. We omitted from consideration GPS data from seven sites nearest the site RENO that were collected after 1 March 2008 because the Mogul seismic swarm in west Reno, Nevada, caused significant nonlinearity to the time series [*Blewitt et al.*, 2008].

### 2.2. GPS Data Processing

[8] The RINEX GPS observation files were processed with the GIPSY-OASIS II software package from the Jet Propulsion Laboratory (JPL) as a part of a global solution that includes over 8000 stations worldwide. Station coordinates were estimated every 24 h using the Precise Point Positioning (PPP) method [*Zumberge et al.*, 1997]. Ionosphere-free combinations of carrier phase and pseudorange were processed every 5 min. The observable model includes ocean tidal loading (including companion tides), estimation of wet zenith troposphere and two gradient parameters as a random walk process using the GMF mapping function, and antenna calibrations for ground receivers and satellite transmitters, and station clocks estimated as a white noise process. We resolved ambiguities in carrier phase across the entire global network by automatic selection of the ionospheric or pseudorange widelane method using the rapid Ambizap algorithm. This technique is based on a fixed point theorem that approximates a full network resolution to better than 1 mm in a global solution [*Blewitt*, 2008]. Satellite orbit and clock parameters were provided by JPL, who determine these parameters in a global fiducial-free analysis using a subset of the available IGS core stations as tracking sites. We deleted positions that were immediately recognizable outliers in the time series, i.e., those with values more than 20 mm from the expected position for each site based on a provisional linear model of the time series, or positions with uncertainties in any ($x$, $y$, or $z$) coordinate greater than 10 mm. The mean formal uncertainty in daily coordinates is 1.1, 1.7, and 1.5 mm in the $x$, $y$, and $z$ coordinates, respectively, and 0.8, 0.5 and 2.2 mm in the north, east, up directions, respectively.

### 2.3. Reference Frame Alignment

[9] The daily GPS solutions were aligned with a reference frame rotating with the rigid interior of NA. Reference frame sites were selected to avoid areas subject to significant postglacial isostatic adjustment (GIA), i.e., are located away from the peripheral bulge associated with GIA. These sites are BRMU, BRTW, DQUA, FBYN, GODE, HAMM, HLFX, JTNT, MACC, MBWW, NPRI, PLTC, PRCO, STJO, WLCI, and WNCI. In the first step daily solutions were aligned to ITRF2005 by applying a seven-parameter Helmert transformation (3 rotations, 3 translations and a scale component) obtained from JPL (sideshow.jpl.nasa.gov). In a subsequent 3 parameter rotation the daily solutions were aligned to minimize the horizontal velocity of these stations. In a third step, 13 long running and stable sites were used to define a seven-parameter spatial filter that removes common mode noise that has a spatial similarity over the span of the Great Basin [*Wdowinski et al.*, 1997]. This type of noise is presumed to be common to all sites in the network and includes daily residual translations of the regional network that might arise from orbit error, for example. The sites chosen to define this filter are ALAM, APEX, ARGU, BULL, DYER, GABB, LIND, MBWW, MDO1, MODB, MONI, RAIL, SNI1.

[10] The resulting frame, which we term "GB09" (based on data through the end of 2009), provides a reference to rigid NA and removes much of the signal from the GPS coordinate time series not attributable to tectonic strain. As a result the time series have less scatter than those in some other NA fixed reference frames that are spatially filtered on larger geographic scales (e.g., The Stable North America Reference Frame (SNARF)) [*Blewitt et al.*, 2005]. Both

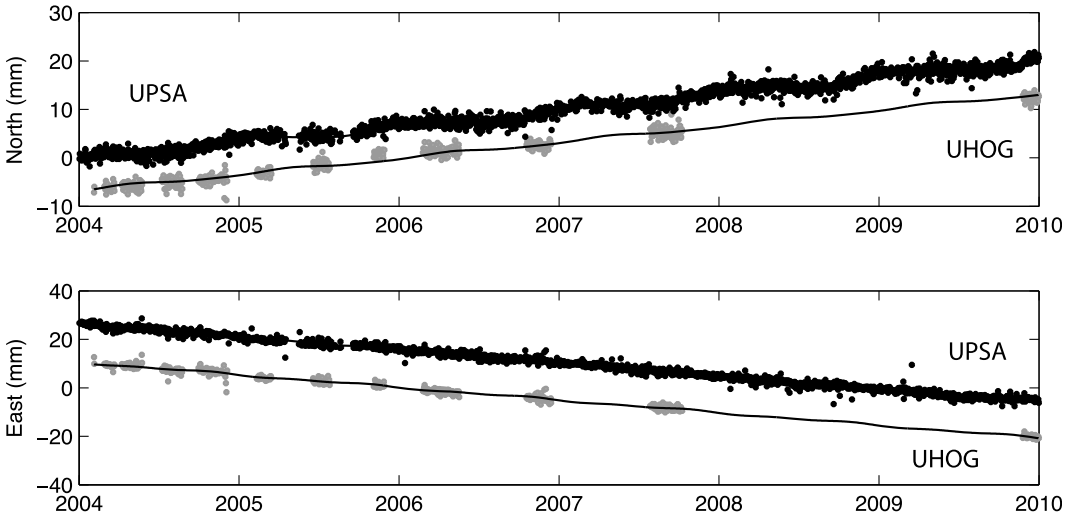


**Figure 2.** (top) North and (bottom) east GPS time series for the BARGEN continuous site UPSA (black) and the MAGNET site UHOG (gray). These sites are collocated within 30 m of one another. A best fitting model with rate, intercept, annual, and semiannual terms is plotted over each time series, which has been offset to facilitate comparison.

MAGNET and continuous sites experience similar reduction in time series scatter resulting in improved resolution of relative rates of motion for GPS stations inside or near the Great Basin. Figure 2 shows time series for two stations in the Carson Sink; UHOG is a MAGNET station located within 30 m of the PBO nucleus station UPSA. Figure 2 illustrates the similarity between time series scatter in the two GPS observation styles and precision to which UHOG tracks the motion of UPSA. The north (east) rates for UHOG and UPSA differ by 0.14 (0.32) mm/yr where the uncertainties in the rates are 0.31 (0.27) mm/yr.

### 2.4. Velocity Estimation

[11] To estimate the velocity field used in this study we use data from 156 MAGNET, 37 PBO, 17 BARGEN, 5 BARD, and 9 Washoe County stations. Of these sites 213 are inside Figure 1, with the remaining sites used to constrain SNGV rigid rotation or for regional filtering. The MAGNET sites in Figure 1 are among the first to be established, since they are among the closest to our offices in Reno, NV, and have the longest occupation history. Owing to this proximity many have been surveyed multiple times per year, for durations of 1–3 months per occupation. We only include sites that have time series at least 2.0 years long, and have velocity uncertainties less than 2 mm/yr.

[12] Rates of motion are estimated from position time series using least squares. We solve for the intercept $\boldsymbol{b}$, rate $\boldsymbol{v}$ and annual and semiannual terms $\boldsymbol{C_i}$ and $\boldsymbol{S_i}$ for $i = 1$ and 2, for each station:

$$\boldsymbol{x}(t) = \boldsymbol{b} + \boldsymbol{v}t + \sum_{j=1,2} \left[\boldsymbol{C}_j \cos(j\omega t) + \boldsymbol{S}_j \sin(j\omega t)\right] + \sum_{k=1}^{M} \left[\boldsymbol{D}_k H(t - t_k)\right]. \quad (1)$$

The terms $\boldsymbol{b}$, $\boldsymbol{v}$, $\boldsymbol{C}_j$, $\boldsymbol{S}_j$ and $\boldsymbol{D}_k$ are 3 × 1 vectors and the $x$, $y$, and $z$ coordinates are contained in $\boldsymbol{x}$. The $x$, $y$, $z$ rates in $\boldsymbol{v}$ are estimated simultaneously so that correlations between $x$, $y$, $z$ rates are estimated. The rates are subsequently transformed into north, east and up rates for tectonic interpretation. The phase of the seasonal terms is allowed to differ across components. The $\boldsymbol{D_k}$ terms are associated with equipment changes for the continuous sites occurring at known times $t_k$. For MAGNET sites there were no offsets attributable to equipment changes since all the equipment is identical, so $\boldsymbol{D_k}$ were not estimated.

[13] For MAGNET sites that had less than 3.0 years of total occupation history, the sampling is limited enough so that solving for rates according to (1) sometimes allows a situation where the annual and semiannual terms are poorly constrained. Therefore, for MAGNET sites with less than 3.0 years of occupation history, we omit the $\boldsymbol{C_i}$ and $\boldsymbol{S_i}$ terms during the rate estimation, and solve only for $\boldsymbol{b}$ and $\boldsymbol{v}$. Rates for all the sites used in this study are shown in Table S1 of the auxiliary material and in Figure 3.[1] For convenience of those using these rates we provide them in ITRF 2005 reference frame as well as in GB09. In Figure 3 the rates are shown both in the GB09 frame, and in a frame where the predicted rotation of the SNGV has been subtracted from the rates at all sites. These rates represent motion with respect to the SNGV and better illustrate the gradients in velocities near its east edge.

[14] Figure 4 shows profiles of the velocities across three transects, whose locations and orientations are shown in Figure 1. These transects can be compared to earlier results of geodetic measurement across the Walker Lane. In one example, *Hammond and Thatcher* [2007, Figures 3e and 3f] showed the results of tripod-based campaign GPS measurements of rates across the Wassuk Fault near Hawthorne, NV in the central Walker Lane. Their campaign results had a scatter that was approximately 2–3 mm/yr, taken as residual

[1] Auxiliary materials are available in the HTML. doi:10.1029/2010JB007817.

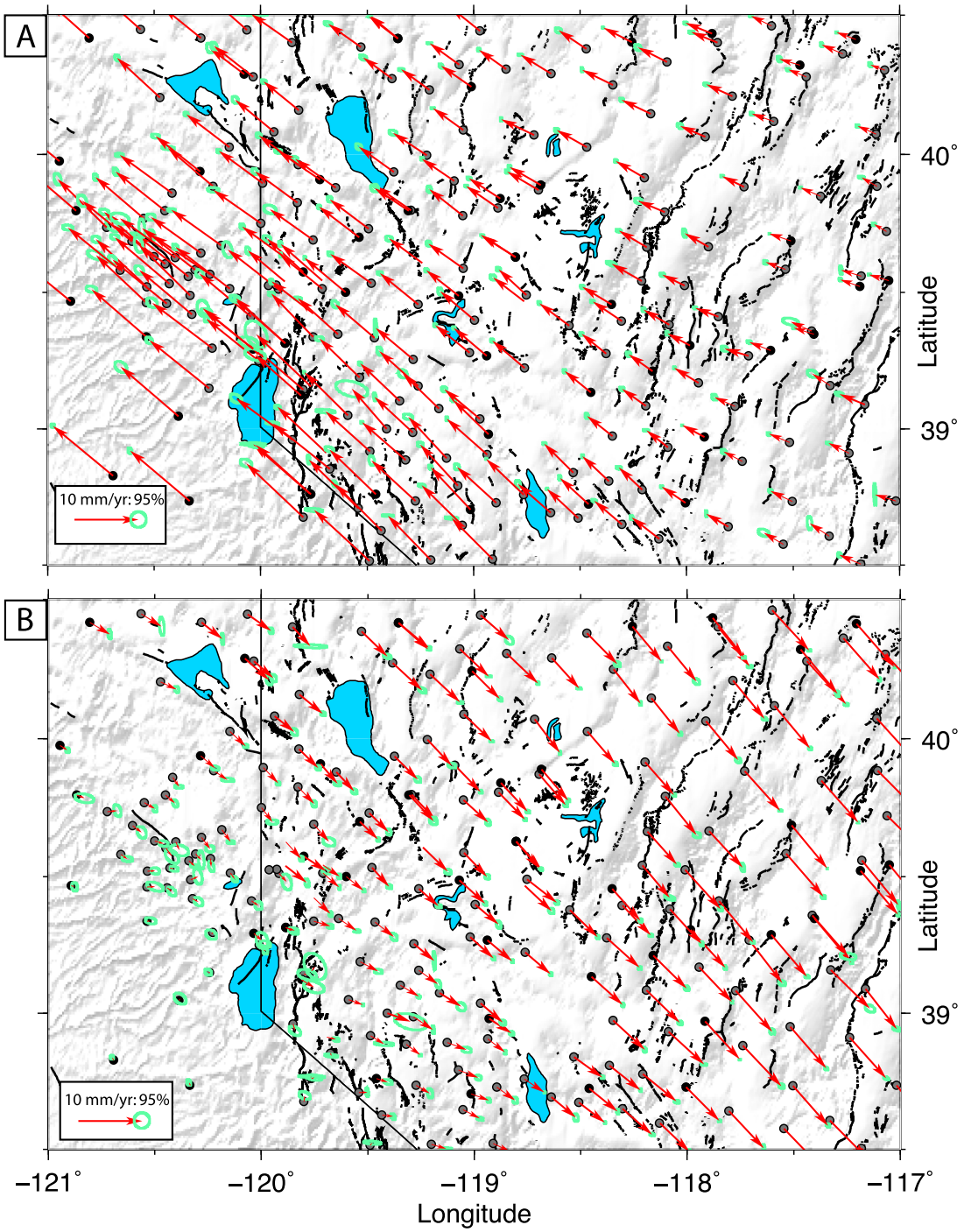


**Figure 3.** GPS Velocity field in (a) North America GB09 reference frame and (b) in a Sierra Nevada/ Great Valley microplate reference frame. Green ellipses indicate the 95% confidence region for each velocity. Gray circles are MAGNET; black circles are continuous stations.

from the trend across directions both parallel and perpendicular to the profiles. Our results here suggest a scatter that is on the order of 0.5 to 1.0 mm/yr (Figures 4a and 4b) taken near the same area across a similar extent of the network. While differences between observation length, directions of the profiles in a varying strain field, etc. may contribute to these difference we believe that they are primarily the result of MAGNET monumentation and occupation strategy, and improvements in GPS data processing methods.

### 2.5. Viscoelastic Correction

[15] When GPS velocities are used to infer long-term deformation of the crust, i.e., the secular motions of blocks and faults slip rates averaged over multiple seismic cycles, it is necessary to correct for the presence of transient motions that distort the velocity field. Such distortions can arise when large earthquakes occur inside or near the study area, and transient deformation associated with viscoelastic

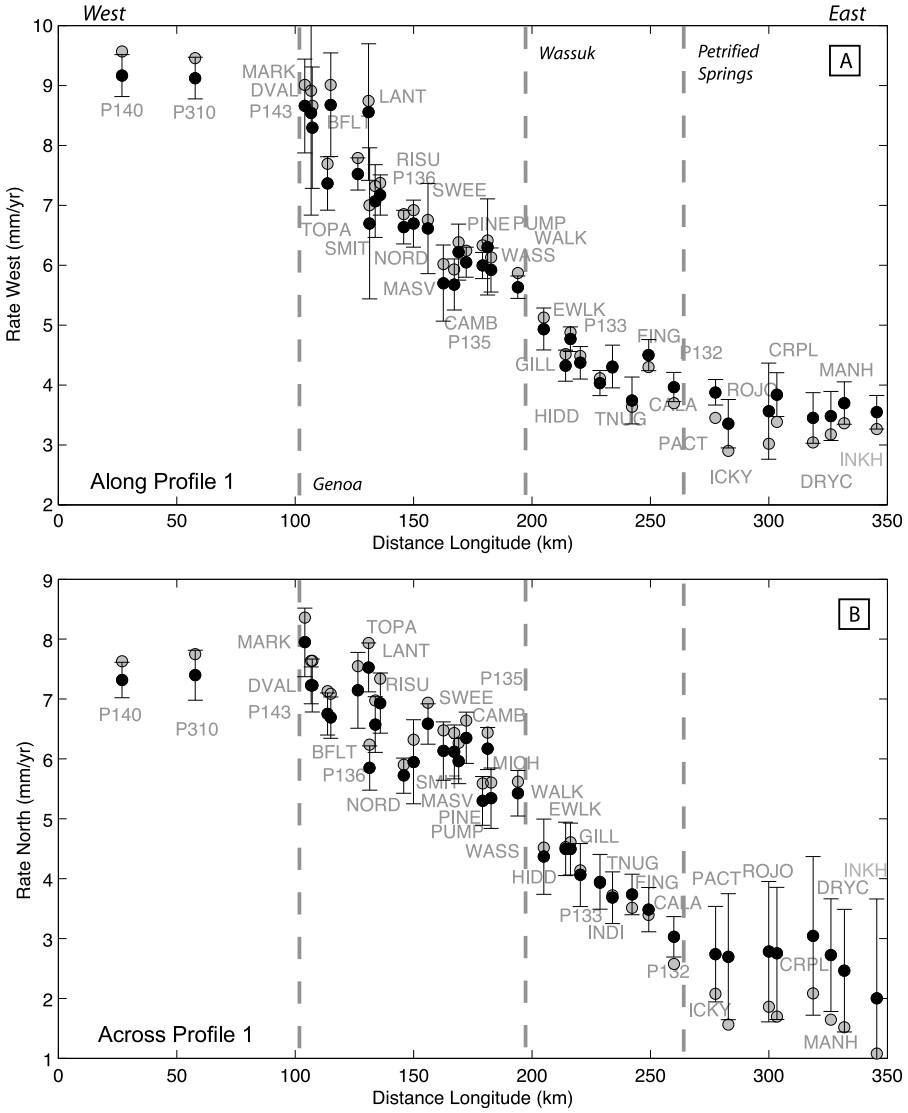


**Figure 4.** (a and b) GPS velocity as a function of distance along profile 1, whose location is shown in Figure 1. Figure 4a is rate along profile, while Figure 4b is rate perpendicular to profile. Black (gray) circles denote rate with (without) correction for postseismic relaxation. Gray dashed lines indicate faults crossed by profile. Names for selected sites are given in gray. (c and d) Same as Figures 4a and 4b, except for profile 2. (e and f) Same as Figures 4a and 4b, except for profile 3.

relaxation continue to occur. It has been shown that viscoelastic models of the earth [*Nur and Mavko*, 1974; *Savage and Prescott*, 1978; *Pollitz et al.*, 2000] explain some features of postearthquake deformation. These effects can persist for weeks to decades after the events and have far-reaching effects [*Freed et al.*, 2007; *Pollitz et al.*, 2008; *Hammond et al.*, 2010]. Using information about the magnitude, location and style of earthquake events it is possible to model viscoelastic effects [*Pollitz*, 1997] in order to separate these transient deformation signals from the that of steady secular strain.

[16] Central Nevada has experienced several large historic earthquakes that have the potential to cause significant transient deformation in the contemporary GPS velocity field. The 1954 Dixie Valley $M_W$ 7.1, 1954 Fairview Peak $M_W$7.1, 1954, Stillwater $M_W$6.8, 1915 Pleasant Valley $M_W$ 7.2 occurred inside the area in Figure 1 and were some of the largest in the Basin and Range in historic time (magnitudes from *Pancha et al.* [2006]). We use the model of *Hammond et al.* [2009] which was specifically designed to adjust the GPS velocity field in our area of interest for the transient effects of these large earthquakes. The correction is largest near the epicenters of the historic earthquakes, reaching 1.5 mm/yr, in opposite directions to the east and west of the epicenters, and close to zero very near, and very far from, the CNSB. Because the relaxation is a diffusion of stress the effects broaden and attenuate over time, decrease toward zero far from the epicenters but are nonzero almost everywhere in the area of interest. We interpolate the model of *Hammond et al.* [2009], which was estimated from an earlier version of the velocity field that included campaign stations from several published studies [*Kreemer et al.*,

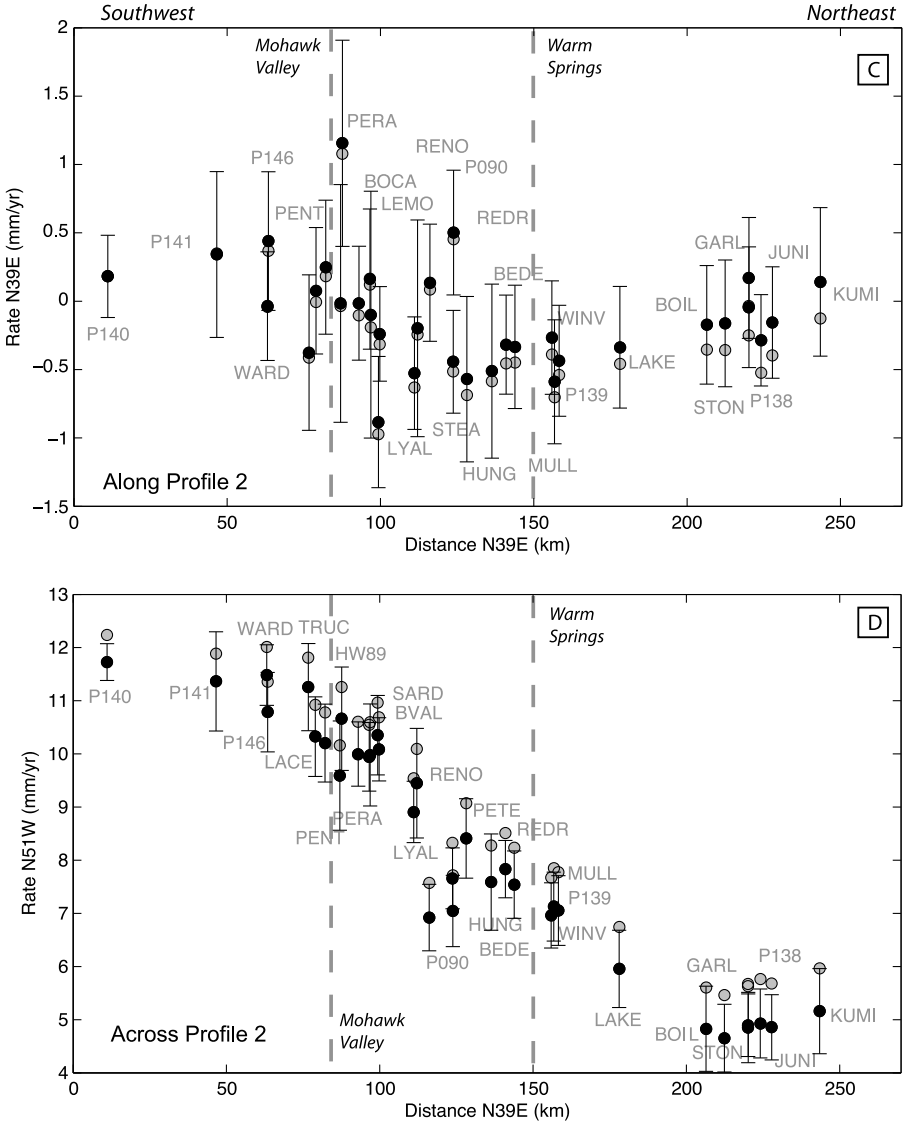


**Figure 4.** (continued)

2009], onto the GPS stations we present here. The velocities of the relaxation model are shown in Figure 5. Velocities both with and without the correction are shown in Figure 4 and are provided in Table S1.

### 2.6. Velocity Uncertainties

[17] Knowledge of the uncertainty in GPS velocities is important in order to understand how much detail in the crustal deformation can be resolved and to quantify the significance of differences between various models. Much study has gone into estimating the uncertainty in rates because formal position uncertainties provided by the GIPSY analysis are likely too small, and the presence of time-correlated noise in the data is demonstrable [e.g., *Agnew*, 1992; *Langbein and Johnson*, 1997; *Williams et al.*, 2004]. Estimating rate uncertainties given the length of the time series, uncertainty of position observations, and knowledge of underlying noise content is possible using the Maximum Likelihood Estimation (MLE) approach [*Mao et al.*, 1999]. A free software (CATS) is available for applying this model to estimate rates and uncertainties in the presence of power law and other types of noise [*Williams*, 2003].

[18] For comparison, we compute uncertainties in two ways. In the first method, we solve for the rate using (1) with data weighted by the one over the variance of the data, and then we scale the uncertainties so that the misfit of the time series model (e.g., (1)) fits with a $\chi^2$ per degrees of freedom of 1. This method compensates for position uncertainties that may be uniformly underestimated by the GIPSY analysis software, and interprets scatter in the time series as noise. In the second method, we include a greater number of potential sources of uncertainty. To account for time-correlated noise we use the CATS software on each time series component to solve (1) with additional terms for the amplitudes for white and flicker noise. We also include uncertainty associated with our viscoelastic correction. We estimate the variance in relaxation model velocities inside

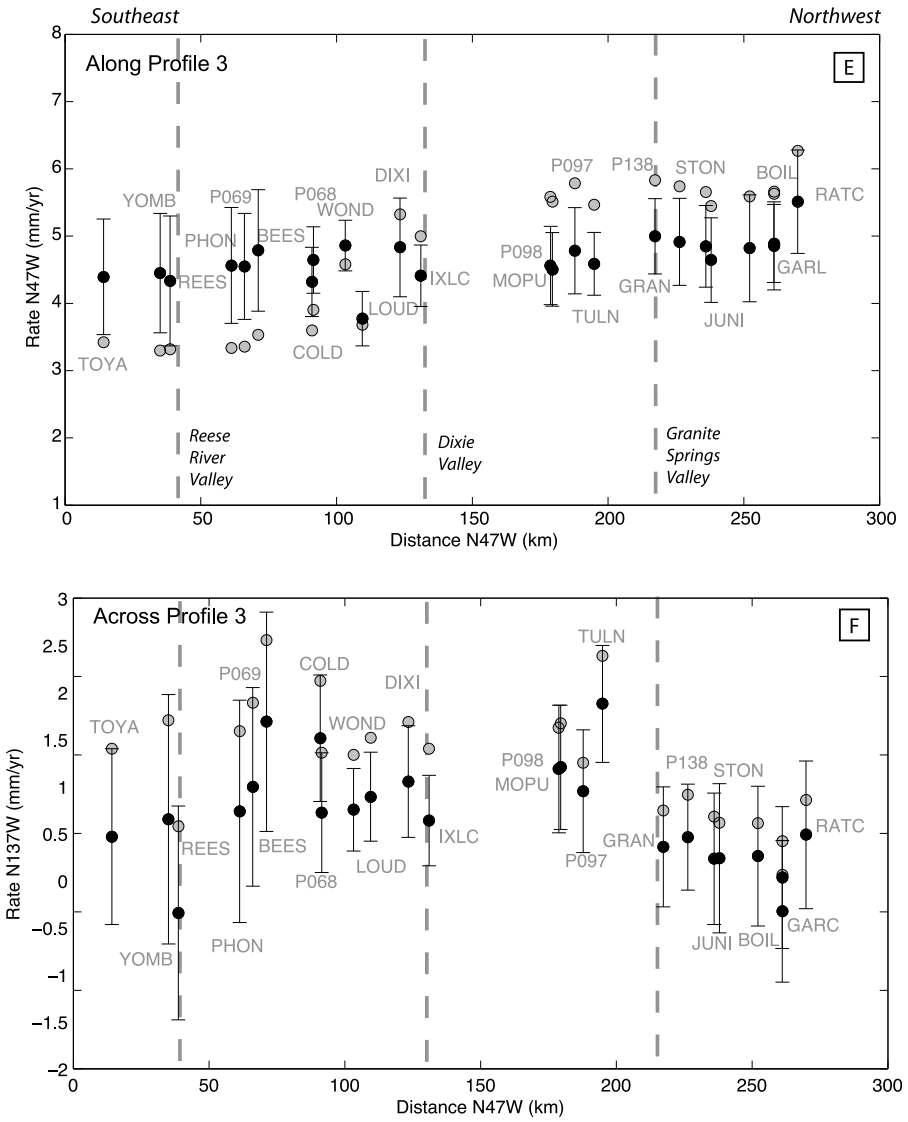


**Figure 4.** (continued)

the set of models with lower crust and upper mantle viscosity values that adequately fit the data in the study of *Hammond et al.* [2009]. This uncertainty is generally a function of distance and direction from the epicenters, is subject to model assumptions about rheology, earthquake parameters, lack of lateral heterogeneity. This contribution to uncertainty is smallest at sites farthest from the epicenters (~0.1 mm/yr) and largest near the epicenters (~0.6 mm/yr). Figure 6 shows that both methods provide uncertainties that decrease with increasing time series length, but that the CATS+postseismic relaxation uncertainties are generally larger by a mean factor of 5.0 (4.8) in the north (east) component. For the remainder of this analysis we use the larger uncertainties since they are likely more realistic.

### 2.7. How Smooth Is the GPS Velocity Field?

[19] Our measurements, made in the interseismic time, reflect the motion of crustal blocks and elastic strain accumulation at their perimeters. We expect that the velocity field, owing to the faults being locked (not slipping) at the surface, will be relatively smooth compared to the geographically discontinuous motions of blocks of crust over geologic time scales. The smoothness of the interseismic velocity field can be appreciated from visual inspection in map view (Figure 3). However, when many sites move at similar rates (e.g., the west half of Figure 3a) it is difficult to see small differences because the similarities are larger. It is also difficult to evaluate velocity field smoothness in the profiles (Figure 4) because they include sites in a zone 50 km wide that may be sampling deformation that varies somewhat across the profiles. Differences are more apparent when the changes are similar in size to the rate magnitudes, e.g., for rates near Lake Tahoe in the SNGV frame (Figure 3b).

[20] To quantitatively evaluate velocity field smoothness, we compare the velocity field to a smoothed version of itself. For each site, we compare the velocity to a value interpolated from neighboring sites. The smoothed velocity is obtained from a linear interpolation inside the triangle defined by the nearest GPS sites to the site of interest.

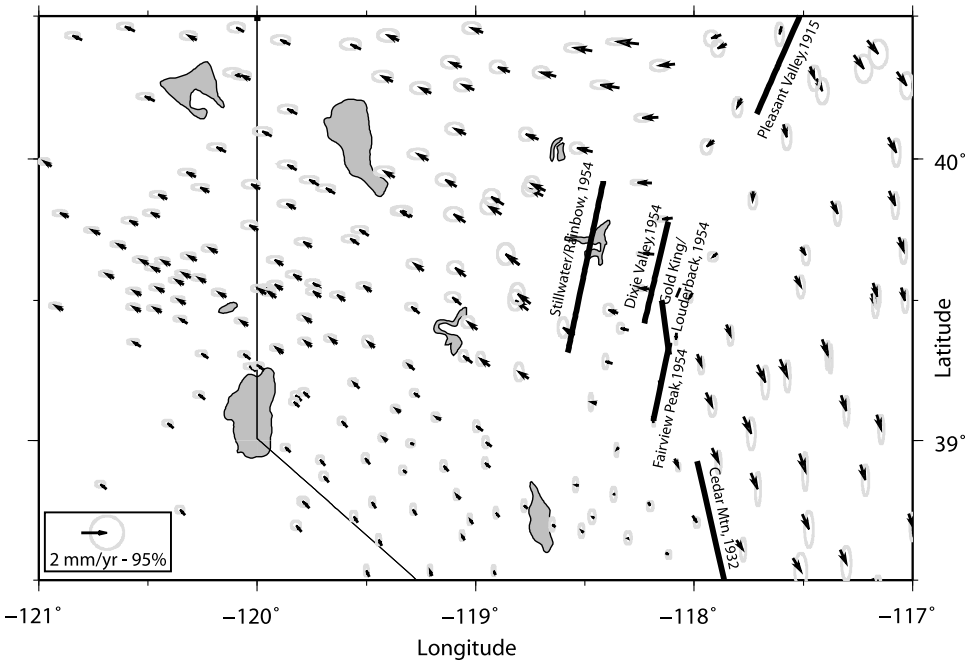


**Figure 5.** Velocities of the correction for postseismic viscoelastic relaxation interpolated from the model of *Hammond et al.* [2009]. Line segments show positions of the surface traces of the historic earthquakes used in the model. Ellipses represent the 95% confidence of the component of uncertainty introduced from viscoelastic relaxation.

Similarity between the velocity and the interpolated velocity represents the amount of redundancy in the measurements. The RMS difference between the velocities and the smoothed velocities is 0.39 mm/yr in the east, and 0.35 mm/yr in the north. Normalized by the uncertainties these values are 1.5 in east and north. If they match exactly for all sites the values would be zero, and if they deviate at a level similar to their uncertainties they would be unity. Since the normalized deviations are greater than one, the data appear not to be systematically redundant. However, the normalized deviations are a function of the uncertainties. If, for example, the uncertainties were increased by a factor of 2.2 in order to explain the misfit between the velocities and block model (discussed below), the velocity field would be smooth in the sense that neighboring velocities are predicted by one another. The conclusion is that if our uncertainties are estimated correctly, then there are additional signals in the velocities that are not explained by the smooth velocity field. Alternatively the velocity uncertainties may still be underestimated despite including contributions from the various understood sources.

## 3. Analysis and Results

### 3.1. Block Modeling

[21] Block modeling is a method by which geodetic measurements made over a few years of interseismic time can be used to infer the motion of blocks of crust over periods of time that are applicable to seismic hazard analysis, i.e., over the next few seismic cycles. This time period is essentially instantaneous in the context of plate tectonics. The analytical details vary somewhat between the different approaches that have been discussed in previous studies [e.g., *Matsu'ura et al.*, 1986; *Bennett et al.*, 1996; *Prawirodirdjo et al.*, 1997; *McClusky et al.*, 2001; *Murray et al.*, 2001; *McCaffrey*, 2002; *Meade and Hager*, 2005; *Reilinger et al.*, 2006; *McCaffrey et al.*, 2007], but are conceptually similar in that they account for block motion and fault locking. These models assume that over many seismic cycles the variation in velocity across the fault is a discontinuous step, but over short times between large earthquakes is a smooth and continuous function owing to fault locking. Block analysis attempts to account for the difference between the long- and short-term velocity field by modeling the elastic strain owing to faults at the block boundaries as vertical or dipping screw dislocations in a half-space [*Savage and Burford*, 1973; *Freund and Barnett*, 1976]. The difference between rigid block motion and smooth interseismic motion is the average rate of motion owing to coseismic slip, which is modeled using the slip on rectangular dislocations that coincide with the shallow seismogenic part of the crust [*Okada*, 1985].

[22] The method we use [*Hammond and Thatcher*, 2007] is conceptually similar to these, is implemented in the MATLAB® software environment, and offers a flexible array of model regularization options. Since it was first described, our method has been enhanced to allow regularization of vertical axis block rotations, and to solve for a constant secular horizontal tensor strain rate of any given block (Appendix A). The problem is structured as a weighted linear inversion with additional constraints that enforce the consistency between relative block motion and slip rates, apply stochastic damping to slip rates, and can constrain slip rates or block rotations to adhere to specific values (e.g., when there is a geologic

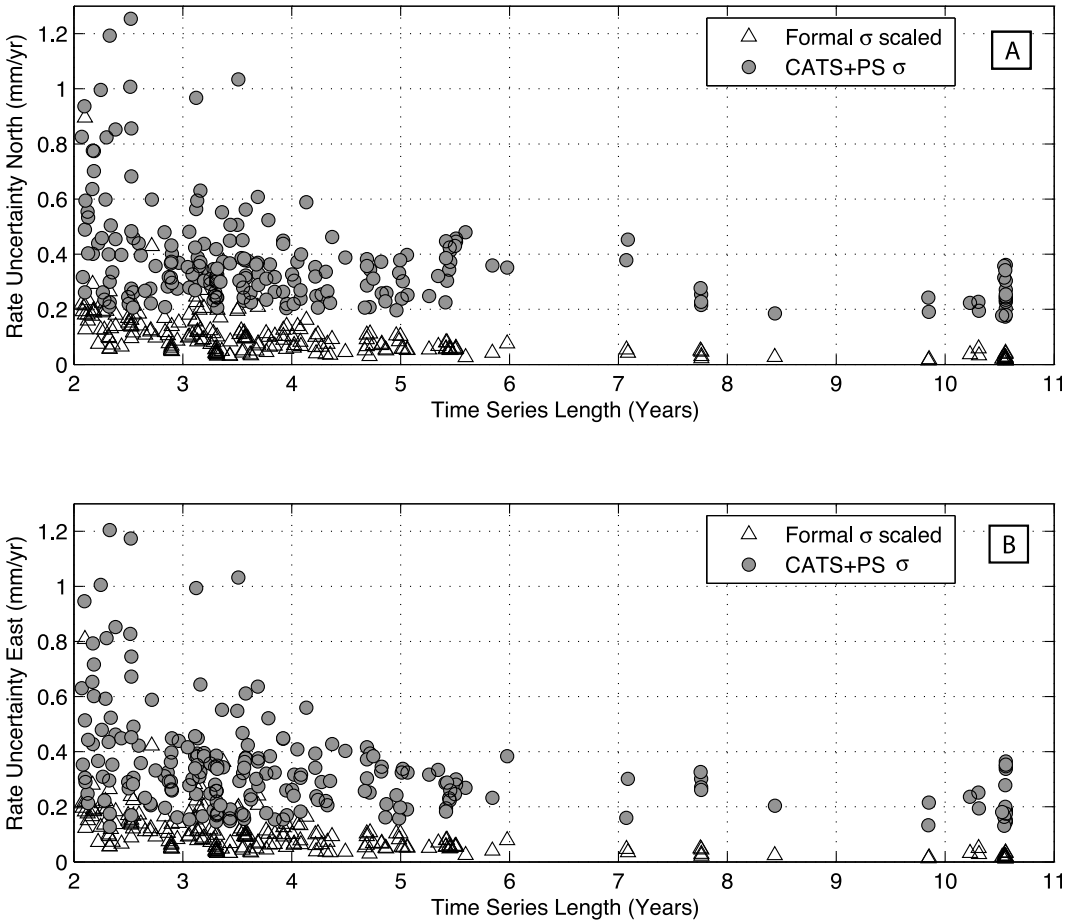


**Figure 6.** Uncertainties in GPS velocities as a function of length of the GPS time series, obtained from formal uncertainties in inversion for rate (triangles) and by adding the combined effects of colored noise [*Williams*, 2003] and the contribution from viscoelastic postseismic relaxation from Figure 5 (circles).

slip rate or plate rotation for which there are other reliable estimates). We hold locking depths and fault dips fixed for each solution.

### 3.2. Geologic Data Constrain Block Geometries

[23] Strain release in the NWL occurs in earthquakes that rupture the surface, and form a complex system of northwest striking dextral, north to north-northeast striking normal and northeast to east-northeast striking sinistral faults (Figure 1). These faults do not share the same degree of continuity and similarity as seen in the San Andreas system to the west. This complexity of faulting has been attributed to several factors, including the relative youth of the system compared to the San Andreas [*Faulds et al.*, 2005], and lesser amount of cumulative slip on each fault [*Wesnousky*, 2005b]. Individual faults in the NWL have 10s to up to 100 km of cumulative offset, much less than the >1000 km on the San Andreas system [e.g., *Howell*, 1976]. Consequently, it can be a challenge to connect NWL block boundaries in ways that honor both the major faults known to accommodate much of the strain, summarize zones of complex and discontinuous faulting, and also adhere to the requirements of kinematic consistency that is required by a block representation.

[24] To construct our model we used fault surface trace data from the USGS Quaternary Fault and Fold database [*U.S. Geological Survey and Nevada Bureau of Mines and Geology*, 2006] to create maps that include the fault traces, topography and patterns of seismicity. The available quantity and density of information from geologic mapping varied considerably inside the region. We used these maps to draw block boundaries that conform to the major active faults, ensuring contiguous blocks. In Figure 7 we show two example details of the block model to illustrate how we developed the model and the level of fidelity that it has to the surface ruptures. For example, in the Tahoe area (Figure 7a) the North Tahoe and Genoa block boundaries adhere very closely to the mapped traces. However, the location of these faults is approximated in places with a few number of straight line segments that summarize multiple mapped traces (e.g., near the southern end of the Genoa fault, and the East Carson Fault Zone). In some cases boundaries are included to represent faults for which activity in the Quaternary is equivocal, e.g., the East Tahoe Fault may not be active. Including such a fault in the model allows flexibility for the analyst to test the effect this fault has on slip rate estimates of other faults. We perform such a test for the East Tahoe fault in the Discussion. In the vicinity of Pyramid Lake (Figure 7b), block boundaries

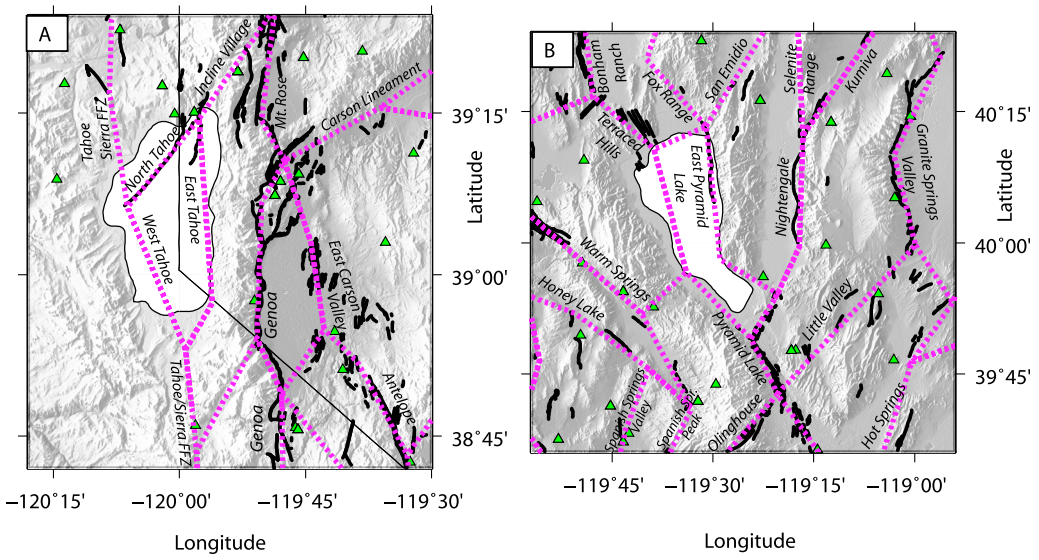


**Figure 7.** Details of block model boundaries (magenta dotted lines), faults (black line segments), and GPS sites (green triangles) for the (a) Tahoe/Genoa/Carson Valley region and (b) Pyramid Lake region. Names of faults are annotated.

follow traces of major faults in the transition between the Basin and Range Province and the Walker Lane dextral transtensional domain. Here most boundaries, including the Pyramid Lake, Olinghouse, Warm Springs, Honey Lake faults follow the mapped traces closely. However, we introduced a fault on the west side of Pyramid Lake in order to connect the Terraced Hills with the Pyramid Lake fault south of the lake, which has the effect of making a separate block beneath the lake. This fault is not required by the observations, but accounts for the possible presence of faults beneath the lake which could be needed to transmit shear deformation between faults systems to the north and south of the lake, without relying on the north striking East Pyramid Lake fault, which appears to be a normal fault. These examples illustrate the type and level of decision making needed in the development of our block model through out the NWL. In many cases, especially in the connections between the long continuous mapped faults, the drawn boundaries necessarily relied somewhat on choices made by the analyst based on the sum of available information including topography, seismicity, and trends in the regional fault strikes and slip styles. Our model is intended to estimate a self-consistent set of slip rates on many faults in the NWL and provide regional context in service to future studies of strain accumulation on the scale of individual faults, basins and ranges. Future data may better delineate blocks and can be used to improve our model geometries. The final model has 60 blocks (Figure 8) and represents a simplification of the fault segments that are known or suspected to be active.

[25] In our model 5 out of the 60 blocks have zero GPS velocities (blocks 5:Tahoe, 19:Pyramid Lake, 20:Smoke Creek, 33:Kumiva, 51:Edwards Creek; Figure 8). They tend to be small, and together account for 2.7% of the area shown in Figure 1. The utility of allowing a block without a GPS site is that in some locations active faults clearly delineate a block, but geodetic measurement of its motion is difficult or not yet complete. For example, the Tahoe block is mostly underwater, though it is bounded on the east and west by faults, some of which are active in the Pleistocene-Holocene [*Kent et al.*, 2005]. In these situations the case for independent block motion is based primarily on geologic observations of faulting. Combining such a block with adjacent blocks would be to assume that a recognized fault is not slipping, which may be inappropriate in light of the evidence for slip. The motion of such blocks in our formulation will be estimated as an average of the surrounding blocks (whose motions generally are constrained by measurement) subject to the damping constraints on slip rate in the inversion. In these cases the slip rates on faults bounding the unconstrained block may not be well estimated, but owing to kinematic consistency the sum of slip rates across profiles that include the unconstrained blocks is well constrained.

[26] We must also assign dips to the faults. Strike slip faults are generally given dips of 80 degrees. Because we do not solve for a component of tensile opening, a dip of 90 degrees would preclude the solution finding any horizontal motion normal to the fault strike. We assigned normal fault dips uniformly to be 45° in the direction either known through seismicity, geologic studies or suggested by the topography. Basin and Range faults are generally considered to dip more steeply than 45° [e.g., *Doser and Smith*, 1989] with some dissent [*Thatcher and Hill*, 1991]. However, by testing many different dips in the block modeling, we find that that there is relatively little sensitivity of the data to fault dip as long as that dip is less than 70° (Figure 9).

### 3.3. Model Regularization and Fit

[27] Because of the number of faults, size of blocks, and incompleteness of GPS data coverage, the models are nonunique and require attention to the regularization. We identify the most likely model by finding solutions that both fit the data and have a minimum amount of structure. Enforcing model simplicity is one way to consider only models that obey our prior expectation that slip styles are similar across fault systems that respond to similar states of lithospheric stress. In other words, we expect similar adjacent faults to slip

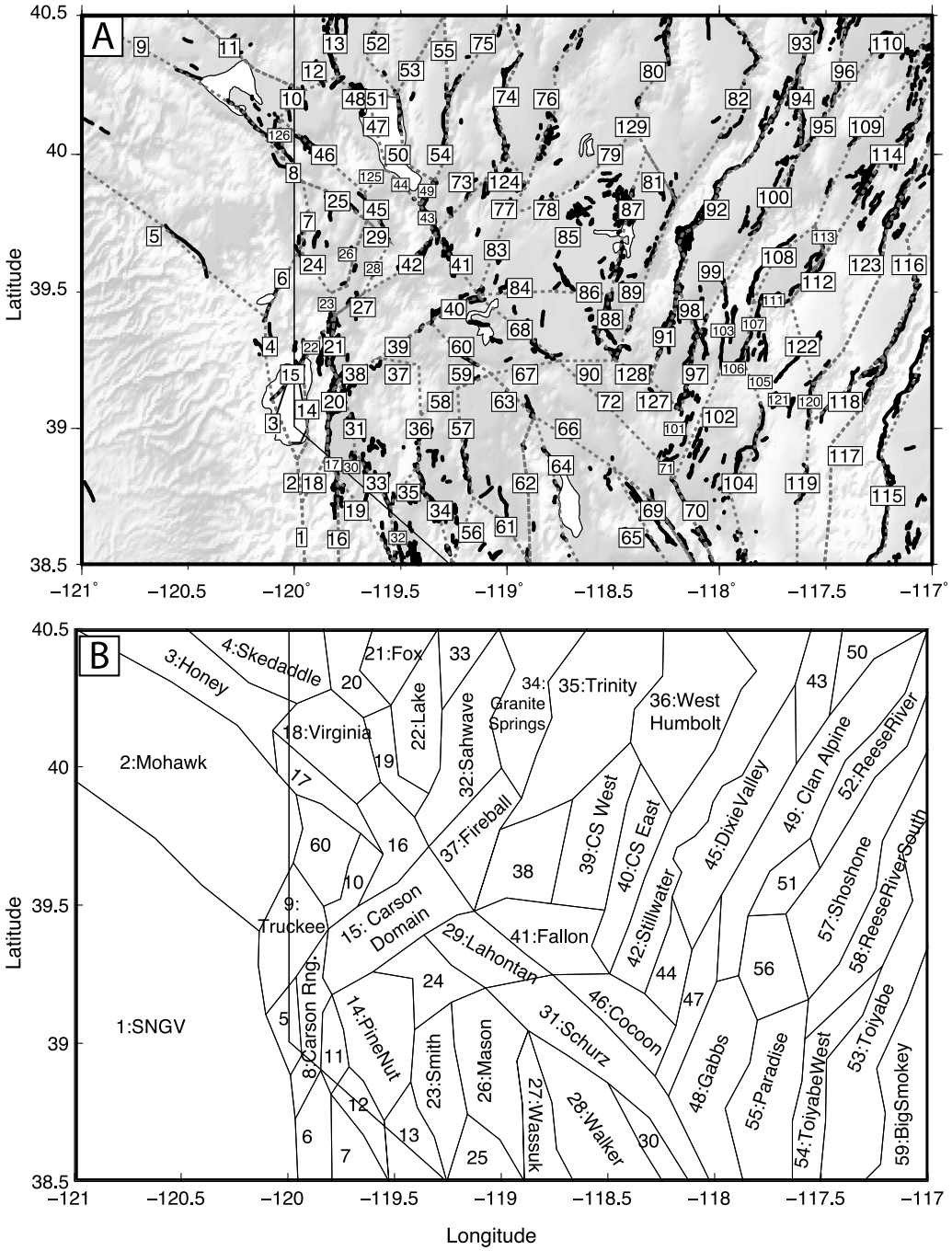


**Figure 8.** Geometry of blocks used in the modeling. (a) Numbers refer to the fault trains, whose slip rates are listed in Table 2, plotted on top of shaded topography and Quaternary faults (black lines) and block boundaries (dotted gray lines). (b) Block names and numbers referred to in text and Table 3.

with similar styles. To regularize the model we use stochastic damping of slip rates and vertical axis spin rates, finding preferred values for prior variance of these parameters in a grid search (Appendix A). We refer to the model in Figures 10a and 10b as our preferred model. In this model slip rates and block translation rates vary somewhat smoothly across the modeling domain. The residual root mean square misfit in the east (west) velocity is 0.43 (0.40) mm/yr, with a $\chi^2$ per degree of freedom of 4.7. The residual velocities are randomly oriented and generally near their uncertainties with normalized misfit of 1.6 (1.7) in the east (north) component (Figure 11). The value of the $\chi^2$ per degree of freedom is made larger by the relatively large number of blocks which increases the number of model parameters and decreases the degrees of freedom. A less smooth model that fits the data more closely is shown in Figure 10c. Here prior uncertainty on slip rates $\gamma$ and vertical axis rotations $\beta$ have been increased to three times the preferred values (Table 1). For this model the residual root mean square misfit in the east (west) velocity is 0.39 (0.32) mm/yr, with a $\chi^2$ per degree of freedom of 3.2. While this model fits the

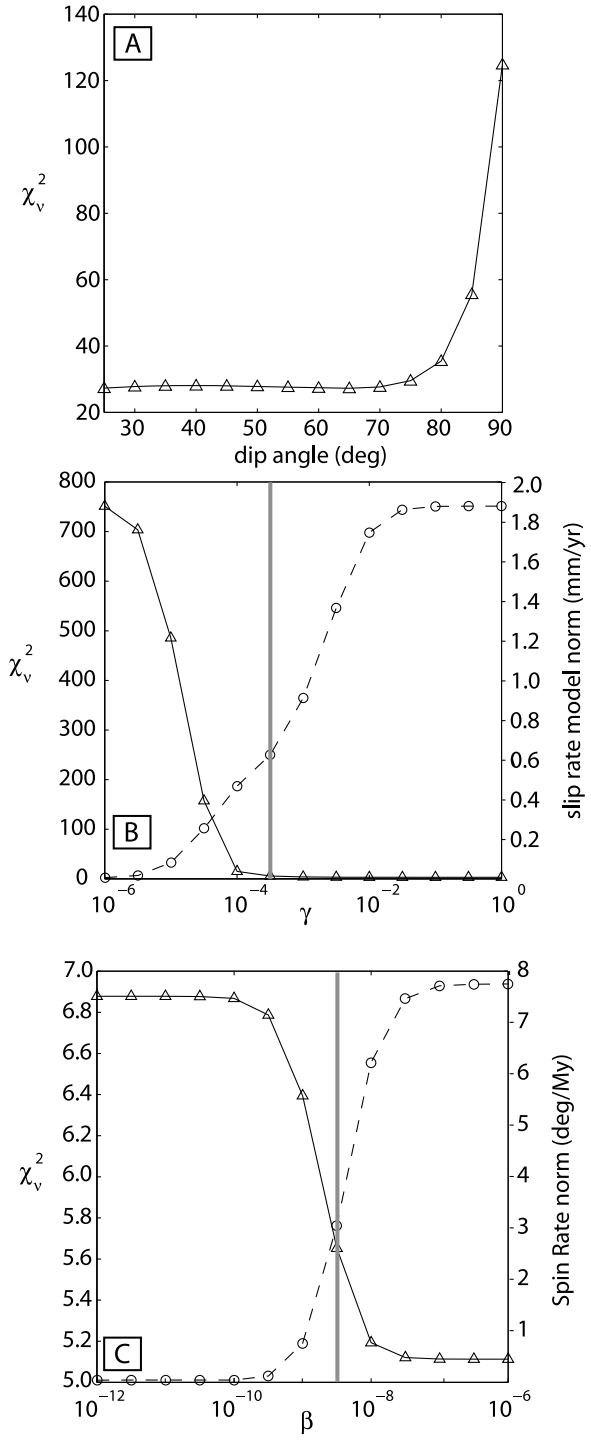


**Figure 9.** (a) Value of model misfit to GPS data as a function of dip of all normal faults in block model. (b) Value of misfit (left vertical axis) and value of model slip rate norm (right vertical axis) as a function of slip rate damping parameter $\gamma$. (c) Value of misfit (left vertical axis) and value of model spin rate norm (right vertical axis) as a function of vertical axis damping parameter $\beta$.

data more closely than the one in Figures 10a and 10b, it shows more random motions in the blocks and is less smooth in the sense that some slip rates across successive fault systems change sign, e.g., near latitude 38.5° along the southern edge of the model. This suggests that the model constraints are too loose, contrary to our guiding principal stated above, and hence we consider the model in Figures 10a and 10b to be more likely. Inspection of our model residuals shows that the sites with the greatest normalized residuals tend to be a combination of those sites with lowest-rate uncertainties, and sites in areas of the largest crustal strain rates. This suggests that the remaining misfit is possibly attributable to a combination of systematic underestimation of the lowest-rate uncertainties, and/or aspects of crustal deformation that are not represented in our model, e.g., if we have not included enough blocks.

[28] Slip rates and uncertainties from the model are provided in Figure 10 and Table 2. Block rotations and their uncertainties are provided in Table 3. The uncertainties in fault slip and block rotation rates are obtained from the formal uncertainty obtained in the solution to the linear system with a further scaling that increases the uncertainties in order to bring the $\chi^2$ per degree of freedom to unity (i.e., by a factor of 2.2). This scaling is applied so that the misfit between the model and data is included in the uncertainty in these parameters, making them more conservative. Faults that bound blocks that have no GPS stations on them are bold in Table 2.

## 4. Discussion

### 4.1. Pattern of Northern Walker Lane Tectonic Deformation

[29] The GPS data confirm a pattern of normal extension across north-south striking normal faults, dextral slip on northwest striking faults, and sinistral slip on east-northeast striking faults, consistent with geological observation. The deformation patterns transition between a few distinct domains characterized by their patterns, rates and styles of fault slip. These domains are the (1) Basin and Range, (2) Walker Lane, (3) Sierra Nevada/Walker Lane transition, and (4) Northern California Shear Zone (Figure 12). For the purpose of discussion of the model fault segments we group faults into sets of consecutive segments that we call fault trains, similar in the sense used by *Bird* [2007]. We define a fault train for each fault segment as the connected sequence of faults that would need to be removed if the two blocks adjacent to the fault were to be combined. The number of each fault train is given in Figure 8a, and mean slip rates are reported for each fault train in Table 2.

#### 4.1.1. Basin and Range

[30] The blocks of the Basin and Range, east of the NWL, move in an average direction of N55W° at an average rate of 4.6 mm/yr relative to North America (Figure 10b). This domain experiences a rate of internal deformation that is small compared to the rate of mean translation. Given that the velocity change along profile 3 is ~1 mm/yr (after the viscoelastic correction, Figure 4e), the mean normal slip rate (projected to the horizontal) across these faults is 0.09 mm/yr, assuming it is distributed evenly over 11 parallel fault systems. In the block model the individual slip rates are predominantly normal, with a few rates estimated to be thrust which could result from mapping noise into small errors in vertical axis rotation rates. The formal uncertainties on individual normal slip rates are typically 0.2 to 0.3 mm/yr, which is generally larger than the individual rates, and none are significantly different than zero. The

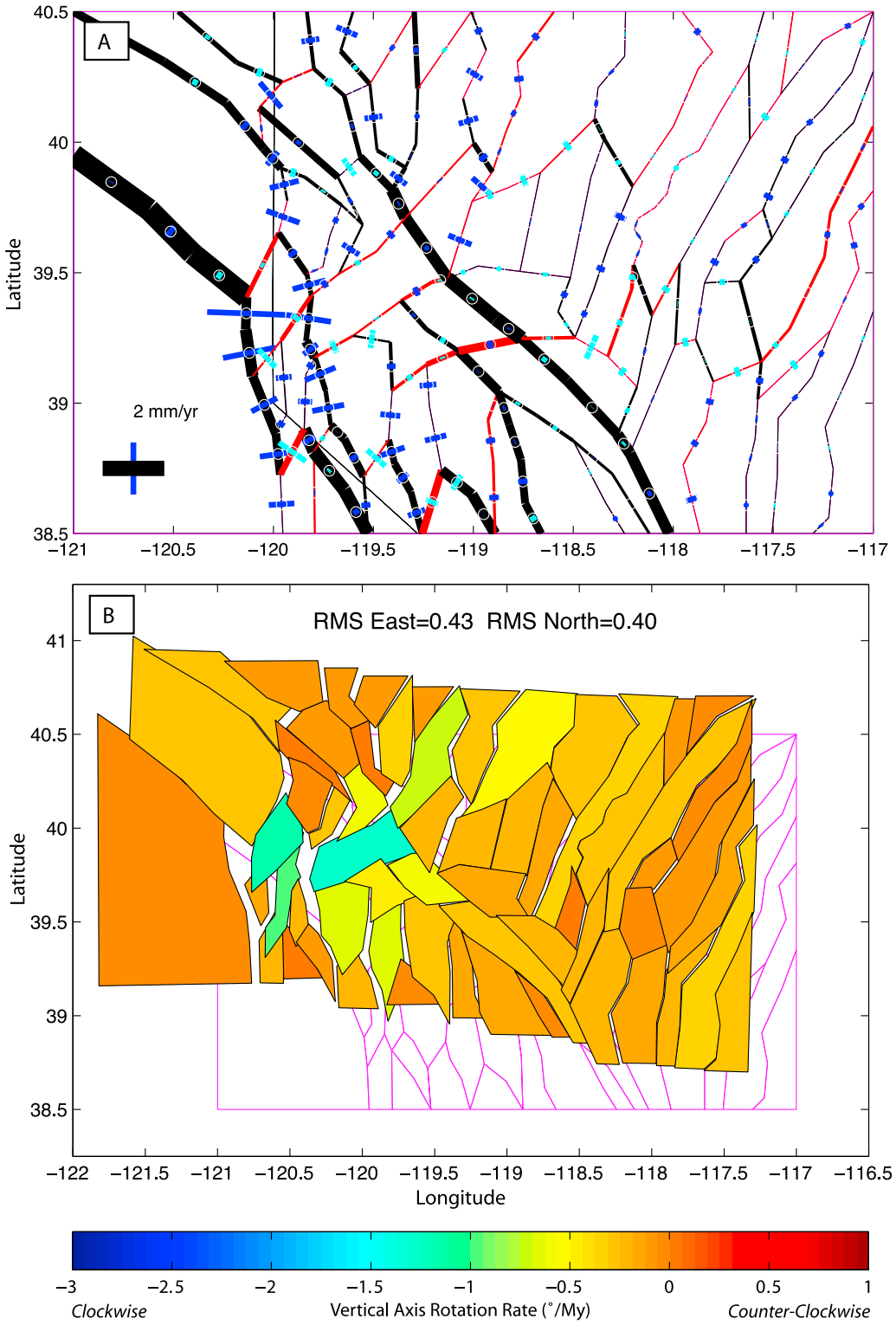


**Figure 10.** (a) Slip rates on faults in our preferred model. Thickness of black (red) line indicates dextral (sinistral) slip rates. Length of fault normal blue (cyan) line indicates normal (thrust) slip rate. (b) Same model except that only the rigid block (long-term) component of motion is shown, exaggerated by a factor of $10^7$. Color of block indicates vertical axis rotation rate. Most rapidly spinning block in cyan color coincides with the Carson Domain of *Cashman and Fontaine* [2000]. (c) Same as in Figure 10b except that $\beta$ and $\gamma$ regularization parameters have been relaxed so their values are three times the values in Table 1.

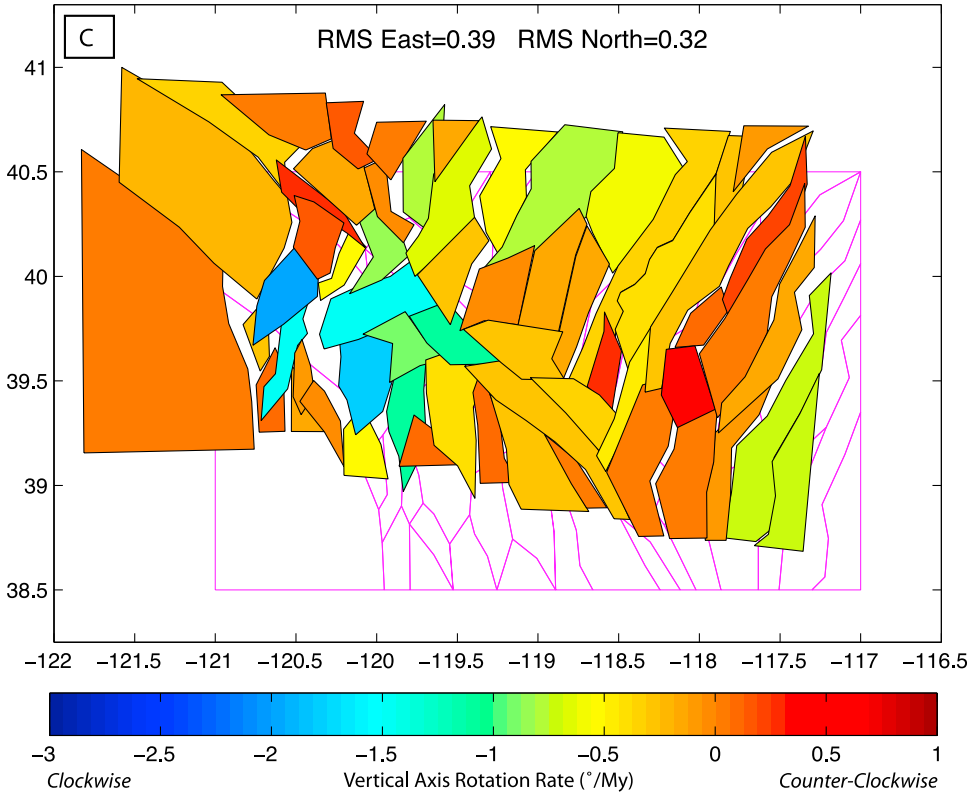


**Figure 10.** (continued)

mean dextral rate on systems in the this domain is 0.0 mm/yr, but vary individually with strike of the individual segments from −0.3 to 0.3 mm/yr.

[31] We make an alternative model where all the blocks of the Basin and Range domain between Pyramid Lake and Big Smokey Valley are combined into a single block, with the horizontal tensor strain rate in this block solved for simultaneously (Figure 13a). This block rotates around a pole located at 47.1 latitude, −110.6° longitude. The strain rates are $4.5 \pm 0.5 \times 10^{-9}$/yr extension directed N78°W, and $3.7 \pm 0.3 \times 10^{-9}$/yr contraction directed N12°E. This model fits the GPS data nearly as well, even though there are only 29 blocks, compared to 60 in the original model, with residual RMS velocity of 0.49 (0.43) mm/yr in north (east) rates, and $\chi^2 = 5.3$. This suggests that the small differences between slip rates we infer in the Basin and Range may not be significant and that the data are mostly consistent with a near-constant deformation across this part of the Province.

#### 4.1.2. Walker Lane

[32] The highest slip rates occur at the east and west margins of the Walker Lane (Figure 3). To the east, as noted previously [*Surpless*, 2008], the highest slip rates are dextral and their location coincides with the system of strike slip faults that includes the Petrified Springs, Benton Springs, Indian Head and Gumdrop faults (Figure 1). This boundary represents a fundamental transition between structural, seismic, and geodetic properties of the Great Basin lithosphere. It coincides with the physiographic eastern boundary of Walker Lane, as suggested by the transition into Basin and Range topography and the boundary of structural domains [*Stewart*, 1988; *Faulds and Henry*, 2008]. The presence of active seismicity [*Goter et al.*, 1994], and also the 1932 Cedar Mountain M 7.1 earthquake [*Doser*, 1988; *Bell et al.*, 1999] are likely responses to the strain accumulation we measure with GPS. The total dextral rate across this zone of transition between the Walker Lane and the Basin and Range is ~2.0 mm/yr. To the northwest of these faults, we have connected the blocks with a northwest striking fault that passes southwest of the Carson Sink, through the Desert Mountains and southwest of the Dead Camel Mountains (Figure 1). The presence of a throughgoing block-bounding fault is not obviously expressed in the active faulting patterns, but strain could be released on mapped faults (e.g., USGS QFFD fault 1674 Unnamed fault zone in Dead Camel, 1310 Unnamed faults in the Terrill Mountains, or 1676 Unnamed faults west of Carson Lake [*U.S. Geological Survey and Nevada Bureau of Mines and Geology*, 2006]), or possibly through oroclinal flexuring that may include a combination of folding or faulting on many smaller structures [*Faulds and Perkins*, 2007; *Faulds and Henry*, 2008]. Northwest of this area this block boundary merges with the Pyramid Lake fault where the dextral slip decreases to 1.0 ± 0.3 mm/yr, and the rest of the dextral slip appears to become distributed among several strike slip and normal faults surrounding the Pyramid Lake area.

[33] The active zone of northwest directed dextral shearing at the eastern edge of the Walker Lane abuts and is kinematically linked to the northwest directed extension of the westernmost Basin and Range province. The model of *Faulds et al.* [2004], suggests that the NWL accommodates

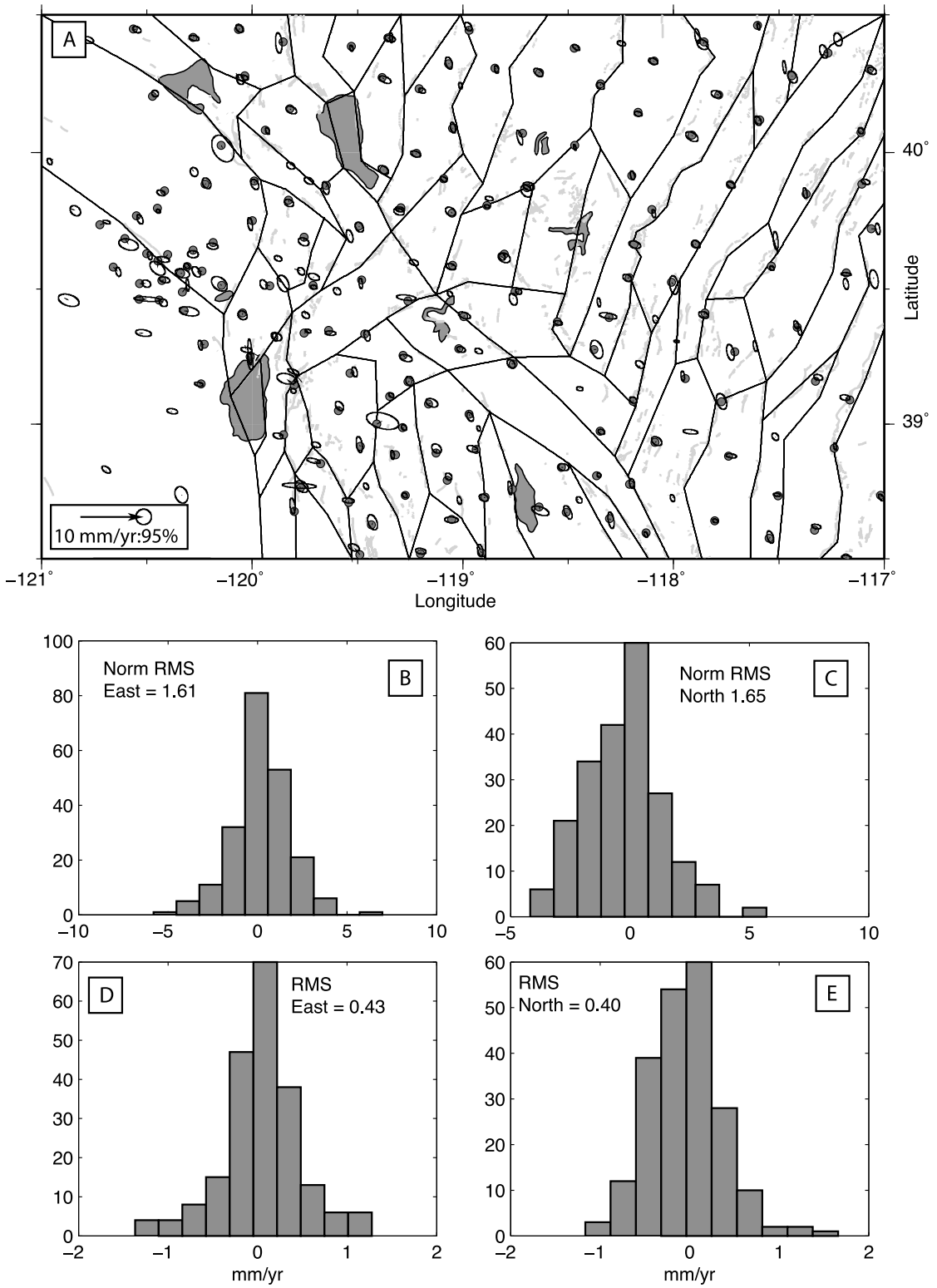


**Figure 11.** (a) Residual GPS velocities after subtracting the predictions of the model in Figures 10a and 10b. Ellipses are 95% confidence areas. (b and c) Histograms of normalized residuals for east and north component, respectively; (d and e) histograms of east and north residuals, respectively.

deformation between the SNGV and northernmost (e.g., Oregon) Basin and Range, which together translate northwest toward Cascadia. Our results are consistent with this model in recognizing that in the Basin and Range as the northwest component of velocity increases to the northwest, this reduces the velocity difference between the Basin and Range and the SNGV. As a consequence the sum of dextral slip rates across the Walker Lane decreases to the northwest.

**Table 1.** Model Assumptions and Regularization

| Type | Value | Units |
|---|---|---|
| Locking depth (L) | 15 | km |
| Poisson's ratio ($\nu$) | 0.25 | - |
| Shear modulus($\mu$) | $3 \times 10^{10}$ | Pa s |
| Slip rate consistency ($\alpha$) | $10^{-6}$ | m $yr^{-1}$ |
| Vertical axis rotation damping ($\beta$) | $3.2 \times 10^{-9}$ | $yr^{-1}$ |
| Slip rate damping ($\gamma$) | $4 \times 10^{-4}$ | m $yr^{-1}$ |

Thus the total amount of shear strain, including cumulative slip on faults, is expected to be less in the NWL compared to the southern Walker Lane. This is not because of a difference in age of initiation between the north and south, but is a geometric consequence of a change in the partitioning between Walker Lane shear and Basin and Range extension in accommodating far-field motion.

#### 4.1.3. Sierra Nevada/Walker Lane Transition Zone

[34] The existence of a distinct Sierra Nevada/Walker Lane Transition zone (SNWLTZ) has been discussed in geologic and seismotectonic studies of NWL structural development [e.g., *Schweickert et al.*, 2004; *Cashman et al.*, 2009]. In many discussions, the westernmost ranges and basins of the Great Basin (e.g., Tahoe and Carson Valley) are specifically excluded from belonging to the Walker Lane [e.g., *Stewart*, 1988; *Cashman and Fontaine*, 2000; *Faulds et al.*, 2005]. The distinctness of this domain is further supported by the rates of deformation that are higher here than elsewhere, as is seen in the greater amount of displacement that has been observed with GPS and portrayed in our block model (Figure 10). Changes in the balance of extension to shear were observed by *Oldow et al.* [2001] in campaign GPS surveys, and interpreted as occupying separate domains of wrench- versus extension-dominated zones of transtension. Our SNWLTZ is narrower than their extension-dominated domain, consisting of the ranges between the Sierra Nevada crest and the Pine Nut Range, but we do confirm greater rates of extension in these westernmost faults. Slip rates across the Tahoe Basin, Genoa, Mt Rose, and Carson fault segments (faults 3, 14, 20, and 31 in Figure 8) sum to 3.7 mm/yr dextral and 2.1 mm/yr normal across this domain. Together these sum to near 40% of the total rate budget across the NWL. Near half of these slip rates are less than the uncertainties, a situation partially attributable to the lack of GPS sites on the Tahoe block, and that the resolution of the model was designed to interpret deformation patterns over a larger region. However, the velocity residuals are no higher in this domain and slip rates are consistent with the pattern of slip prevalent in Walker Lane.

[35] Some studies have found that the SNWLTZ faults around Lake Tahoe lie in a predominantly east-west extensional domain [e.g., *Surpless*, 2008], but our data suggest that the deformation is more dextral than extensional. The southern edge of the model in Figure 10b shows the increase of the north component of block translation with westward distance across the model, indicating that dextral shear strain rates and dextral slip rates for north and north-northwest striking faults increase westward. How this shear is released across the faults in this domain is poorly understood since most observations of surface rupture indicate vertical displacements on normal faults [e.g., *Ramelli et al.*, 1999; *Schweickert et al.*, 2000; *Kent et al.*, 2005]. However, this is a pattern that is consistent across many of the apparently normal fault-bounded grabens and is consistent with the regional pattern of shear-dominated transtension throughout the Walker Lane.

[36] It has been suggested that the transtensional deformation in the Walker Lane is a response of the NWL crust to a misalignment of the SNGV/NWL boundary with northwest motion of the rigid SNGV microplate [*Unruh et al.*, 2003]. This effect may help explain the distinctness of the SNWLTZ because the releasing transtensional geometry is especially pronounced to the south of a line projecting southeast along the Mohawk Valley fault. This is where the eastern boundary of the SNGV changes strike from northwest along the Mohawk Valley fault to north-northwest through the Lake Tahoe Basin and southward (Figure 1). This trend may induce a stress shadow that leaves Tahoe/NWL crust in the wake of SNGV motion, allowing for more rapid extension inside the SNWLTZ.

#### 4.1.4. Northern California Shear Zone

[37] North of our SNWLTZ lies a domain we refer to as the Northern California Shear Zone (NCSZ), following terminology suggested by *Wesnousky* [2005a]. This part of the NWL includes the single largest fault slip rate in the model on the boundary between the SNVG and the block immediately to the northeast (2:Mohawk; Figure 8). In earlier geodetic studies movement on the Mohawk Valley fault was estimated to be 3–9 mm/yr, with geographically sparse continuous and less precise campaign GPS rates responsible for the relatively large uncertainties [*Dixon et al.*, 2000; *Hammond and Thatcher*, 2007]. We have estimated a dextral rate of 2.9 ± 0.2 mm/yr. The uncertainty is low because of the combined strength of continuous sites that constrain the SNGV, and the number of sites on the Mohawk block. The horizontal extension rate normal to the fault is 0.1 ± 0.1, consistent with predominantly strike slip strain accumulation.

[38] Another fault in this domain is the Honey Lake fault, which is similar to the Mohawk Valley fault in that it shows a geodetic signature of a dextral strike slip fault. We estimate a dextral slip rate of 1.2 ± 0.3 mm/yr and a normal rate (horizontal extension) of 0.1 ± 0.2 mm/yr. A less studied, and possibly less developed, strike slip fault parallel to these faults is the Grizzly Valley fault, which was not included in our model. Because these are three subparallel faults and accommodate the same style of strain accumulation, some trade-off between slip on these faults may exist, so the formal uncertainties are likely too low. The implications of various possibilities for fault geometry, dip, and cross-fault variation in material properties is currently underway in a separate detailed study (http://earthquake.usgs.gov/research/external/reports/08HQGR0027.pdf).

### 4.2. Vertical Axis Rotations

[39] Vertical axis rotations in the model indicate a transition from a counterclockwise rotating SNGV block at the western edge of the model, to almost all other blocks rotating clockwise (Figure 10b). Rotation of the northern half of the SNGV is very well constrained by GPS sites. We see in Figure 3b that the three PBO sites not used in the definition of the SNGV (P141, P144, P146) have zero velocity with respect to the SNGV, and thus show that it is rigid nearly to the Sierra Nevada crest. Throughout the rest of the model vertical axis spin rates are generally less

**Table 2.** Fault Slip Rates From the GPS-Only Block Model[a]

| Fault Train | Strike Slip Rate (mm/yr) | Dip Slip Rate (mm/yr) | Horizontal Extension (mm/yr) | Fault Number |
|---|---|---|---|---|
| 1 | 0.00 ± 0.34 | −0.82 ± 0.39 | −0.58 ± 0.28 | 1 |
| 2 | −1.12 ± 0.21 | −1.23 ± 0.33 | −0.87 ± 0.23 | 2 |
| **3** | **−1.23 ± 0.33** | **−0.98 ± 0.41** | **−0.69 ± 0.29** | **3** |
| 4 | −1.39 ± 0.22 | −2.29 ± 0.23 | −1.62 ± 0.16 | 4, 5 |
| 5 | −2.85 ± 0.12 | −0.35 ± 0.36 | −0.06 ± 0.06 | 6, 7, 8 |
| 6 | 0.61 ± 0.24 | 0.49 ± 0.56 | 0.08 ± 0.10 | 9 |
| 7 | −0.13 ± 0.18 | −1.15 ± 0.26 | −0.81 ± 0.18 | 10, 11 |
| 8 | −1.15 ± 0.27 | −0.60 ± 0.22 | −0.43 ± 0.15 | 12 |
| 9 | −1.16 ± 0.27 | 0.08 ± 0.35 | 0.05 ± 0.24 | 13, 14, 219 |
| 10 | 0.29 ± 0.28 | −1.17 ± 0.39 | −0.83 ± 0.28 | 15 |
| 11 | −0.66 ± 0.29 | 0.21 ± 0.40 | 0.15 ± 0.28 | 16, 17 |
| 12 | 0.29 ± 0.33 | −0.12 ± 0.67 | −0.02 ± 0.12 | 18 |
| **13** | **−0.50 ± 0.35** | **−0.64 ± 0.48** | **−0.45 ± 0.34** | **19** |
| **14** | **−0.12 ± 0.34** | **−0.40 ± 0.40** | **−0.28 ± 0.29** | **20, 21** |
| **15** | **0.27 ± 0.37** | **0.86 ± 0.43** | **0.61 ± 0.30** | **22** |
| 16 | 0.26 ± 0.45 | −0.03 ± 0.51 | −0.02 ± 0.36 | 23 |
| 17 | −1.70 ± 0.39 | −0.46 ± 0.47 | −0.32 ± 0.33 | 24 |
| 18 | 0.84 ± 0.36 | 1.16 ± 0.44 | 0.82 ± 0.31 | 25 |
| 19 | −1.75 ± 0.37 | −0.06 ± 0.46 | −0.04 ± 0.33 | 26, 27 |
| 20 | −0.11 ± 0.31 | −0.37 ± 0.36 | −0.26 ± 0.25 | 28, 29 |
| 21 | −1.03 ± 0.22 | −1.09 ± 0.30 | −0.77 ± 0.21 | 30, 31 |
| 22 | 0.58 ± 0.31 | 1.21 ± 0.48 | 0.21 ± 0.08 | 32 |
| 23 | −0.63 ± 0.23 | −1.20 ± 0.31 | −0.85 ± 0.22 | 33 |
| 24 | −0.82 ± 0.21 | −0.33 ± 0.34 | −0.24 ± 0.24 | 34 |
| 25 | −0.46 ± 0.28 | 0.33 ± 0.39 | 0.14 ± 0.12 | 35, 38 |
| 26 | −0.03 ± 0.17 | −0.22 ± 0.36 | −0.09 ± 0.15 | 36, 37, 39 |
| 27 | 0.26 ± 0.23 | −0.87 ± 0.55 | −0.15 ± 0.10 | 40 |
| 28 | −0.28 ± 0.18 | −0.69 ± 0.22 | −0.49 ± 0.15 | 41 |
| 29 | −0.31 ± 0.30 | −0.05 ± 0.61 | −0.01 ± 0.11 | 42 |
| 30 | 0.23 ± 0.35 | 0.16 ± 0.46 | 0.12 ± 0.32 | 43 |
| 31 | −0.67 ± 0.29 | −1.15 ± 0.37 | −0.81 ± 0.26 | 44, 45 |
| 32 | −0.39 ± 0.38 | −0.33 ± 0.44 | −0.23 ± 0.31 | 46 |
| 33 | −1.11 ± 0.30 | −0.15 ± 0.39 | −0.11 ± 0.27 | 47, 48 |
| 34 | −0.94 ± 0.28 | −0.69 ± 0.36 | −0.49 ± 0.26 | 49, 50, 51 |
| 35 | 0.25 ± 0.33 | 0.84 ± 0.37 | 0.60 ± 0.26 | 52 |
| 36 | −0.04 ± 0.24 | −0.71 ± 0.31 | −0.50 ± 0.22 | 53 |
| 37 | −0.38 ± 0.20 | 0.16 ± 0.29 | 0.12 ± 0.20 | 54215 |
| 38 | 0.37 ± 0.26 | 1.89 ± 0.58 | 0.33 ± 0.10 | 55 |
| 39 | 0.28 ± 0.22 | 0.28 ± 0.54 | 0.05 ± 0.09 | 56 |
| 40 | 0.51 ± 0.23 | −0.50 ± 0.51 | −0.09 ± 0.09 | 57, 58 |
| 41 | −1.51 ± 0.25 | −0.04 ± 0.57 | −0.01 ± 0.10 | 59 |
| 42 | 0.28 ± 0.22 | −0.25 ± 0.50 | −0.04 ± 0.09 | 60, 61 |
| 43 | −1.67 ± 0.27 | −0.29 ± 0.58 | −0.05 ± 0.10 | 62 |
| **44** | **−1.03 ± 0.30** | **0.63 ± 0.62** | **0.11 ± 0.11** | **63** |
| 45 | −0.36 ± 0.27 | −0.57 ± 0.56 | −0.10 ± 0.10 | 64 |
| 46 | −0.95 ± 0.29 | −0.62 ± 0.51 | −0.11 ± 0.09 | 65 |
| **47** | **−0.61 ± 0.30** | **−0.42 ± 0.64** | **−0.07 ± 0.11** | **66** |
| **48** | **−0.55 ± 0.34** | **0.34 ± 0.44** | **0.24 ± 0.31** | **67** |
| **49** | **−0.58 ± 0.20** | **−0.68 ± 0.38** | **−0.48 ± 0.27** | **68** |
| **50** | **−0.46 ± 0.30** | **−0.21 ± 0.37** | **−0.15 ± 0.26** | **69, 70** |
| **51** | **−0.05 ± 0.33** | **−0.01 ± 0.48** | **−0.01 ± 0.34** | **71** |
| **52** | **−0.51 ± 0.37** | **−0.39 ± 0.48** | **−0.28 ± 0.34** | **72, 73** |
| 53 | 0.18 ± 0.46 | −0.15 ± 0.51 | −0.11 ± 0.36 | 74 |
| 54 | −0.37 ± 0.31 | −0.02 ± 0.36 | −0.01 ± 0.26 | 75, 76 |
| **55** | **−0.70 ± 0.48** | **−0.20 ± 0.56** | **−0.14 ± 0.40** | **77** |
| 56 | 1.00 ± 0.30 | 0.46 ± 0.42 | 0.32 ± 0.30 | 78 |
| 57 | −0.10 ± 0.18 | −0.68 ± 0.31 | −0.48 ± 0.22 | 79, 80 |
| 58 | 0.43 ± 0.29 | 0.82 ± 0.51 | 0.14 ± 0.09 | 81 |
| 59 | 0.73 ± 0.24 | 0.31 ± 0.61 | 0.05 ± 0.11 | 82 |
| 60 | −0.63 ± 0.16 | 0.22 ± 0.54 | 0.04 ± 0.09 | 83, 84 |
| 61 | −1.38 ± 0.29 | 0.27 ± 0.43 | 0.20 ± 0.14 | 85, 86 |
| 62 | 0.39 ± 0.21 | −0.25 ± 0.34 | −0.18 ± 0.24 | 87, 88, 89 |
| 63 | −1.27 ± 0.19 | −0.14 ± 0.58 | −0.02 ± 0.10 | 90 |
| 64 | −1.05 ± 0.23 | −0.07 ± 0.32 | −0.05 ± 0.23 | 91, 92, 93, 94 |
| 65 | −0.15 ± 0.28 | 0.12 ± 0.53 | 0.02 ± 0.09 | 95, 96 |
| 66 | −0.48 ± 0.25 | 0.45 ± 0.44 | 0.08 ± 0.08 | 97, 98 |
| 67 | 1.08 ± 0.22 | −1.13 ± 0.51 | −0.20 ± 0.09 | 99 |
| 68 | −1.88 ± 0.23 | 0.03 ± 0.52 | 0.01 ± 0.09 | 100, 101 |
| 69 | −0.37 ± 0.28 | −0.06 ± 0.51 | −0.01 ± 0.09 | 102, 103 |
| 70 | −1.46 ± 0.24 | −0.64 ± 0.50 | −0.11 ± 0.09 | 104 |
| 71 | −1.50 ± 0.32 | 0.37 ± 0.65 | 0.07 ± 0.11 | 105 |
| 72 | −1.35 ± 0.23 | 0.39 ± 0.52 | 0.07 ± 0.09 | 106, 107 |

**Table 2.** (continued)

| Fault Train | Strike Slip Rate (mm/yr) | Dip Slip Rate (mm/yr) | Horizontal Extension (mm/yr) | Fault Number |
|---|---|---|---|---|
| 73 | 0.23 ± 0.24 | −0.26 ± 0.55 | −0.04 ± 0.10 | 108 |
| 74 | −0.18 ± 0.27 | −0.54 ± 0.35 | −0.38 ± 0.25 | 109, 110, 211 |
| **75** | **0.16 ± 0.47** | **0.14 ± 0.54** | **0.10 ± 0.38** | **111** |
| 76 | 0.22 ± 0.26 | −0.23 ± 0.34 | −0.16 ± 0.24 | 112, 113, 114, 115 |
| 77 | 0.18 ± 0.26 | −0.94 ± 0.37 | −0.67 ± 0.26 | 116 |
| 78 | 0.12 ± 0.24 | 0.37 ± 0.33 | 0.26 ± 0.23 | 117, 118 |
| 79 | 0.19 ± 0.24 | 0.41 ± 0.30 | 0.29 ± 0.21 | 119 |
| 80 | −0.06 ± 0.26 | −0.07 ± 0.32 | −0.05 ± 0.23 | 120, 121, 122 |
| 81 | −0.49 ± 0.28 | 0.01 ± 0.55 | 0.00 ± 0.10 | 123 |
| 82 | 0.13 ± 0.22 | −0.05 ± 0.31 | −0.03 ± 0.22 | 124, 125, 126, 127 |
| 83 | 0.18 ± 0.23 | −0.88 ± 0.30 | −0.62 ± 0.21 | 128 |
| 84 | −0.04 ± 0.19 | 0.02 ± 0.57 | 0.00 ± 0.10 | 129, 130 |
| 85 | −0.07 ± 0.17 | −0.16 ± 0.54 | −0.03 ± 0.09 | 131 |
| 86 | −0.05 ± 0.23 | 0.60 ± 0.58 | 0.10 ± 0.10 | 132 |
| 87 | −0.12 ± 0.18 | −0.13 ± 0.59 | −0.02 ± 0.10 | 133, 134 |
| 88 | −0.24 ± 0.20 | −0.06 ± 0.31 | −0.04 ± 0.22 | 135, 139 |
| 89 | −0.16 ± 0.21 | −0.31 ± 0.31 | −0.22 ± 0.22 | 136, 137, 138 |
| 90 | 0.47 ± 0.26 | 0.44 ± 0.61 | 0.08 ± 0.11 | 140 |
| 91 | 0.47 ± 0.26 | 0.24 ± 0.32 | 0.17 ± 0.23 | 141, 142 |
| 92 | 0.04 ± 0.18 | −0.01 ± 0.24 | −0.01 ± 0.17 | 143, 144, 145, 146, 147 |
| 93 | −0.16 ± 0.35 | 0.06 ± 0.45 | 0.04 ± 0.32 | 153 |
| 94 | −0.24 ± 0.35 | −0.07 ± 0.45 | −0.05 ± 0.32 | 154 |
| 95 | 0.12 ± 0.36 | 0.28 ± 0.42 | 0.20 ± 0.30 | 155 |
| 96 | 0.16 ± 0.43 | 0.08 ± 0.52 | 0.05 ± 0.37 | 156 |
| 97 | −0.18 ± 0.30 | −0.10 ± 0.36 | −0.07 ± 0.26 | 157 |
| 98 | −0.55 ± 0.31 | −0.03 ± 0.58 | −0.01 ± 0.10 | 158 |
| 99 | 0.27 ± 0.26 | 0.28 ± 0.40 | 0.20 ± 0.28 | 159 |
| 100 | −0.02 ± 0.23 | 0.07 ± 0.30 | 0.05 ± 0.21 | 160, 161 |
| 101 | −0.29 ± 0.21 | 0.17 ± 0.37 | 0.12 ± 0.26 | 162 |
| 102 | −0.07 ± 0.22 | −0.06 ± 0.32 | −0.04 ± 0.22 | 163 |
| 103 | −0.32 ± 0.24 | 0.03 ± 0.40 | 0.02 ± 0.28 | 164 |
| 104 | 0.11 ± 0.23 | −0.31 ± 0.35 | −0.22 ± 0.25 | 165, 166, 167 |
| 105 | −0.28 ± 0.28 | 0.08 ± 0.64 | 0.01 ± 0.11 | 168 |
| 106 | 0.15 ± 0.29 | 1.25 ± 0.59 | 0.22 ± 0.10 | 169 |
| 107 | −0.01 ± 0.25 | −0.12 ± 0.36 | −0.08 ± 0.26 | 170 |
| **108** | **0.00 ± 0.30** | **−0.22 ± 0.37** | **−0.16 ± 0.26** | **171, 172** |
| 109 | −0.16 ± 0.24 | −0.14 ± 0.33 | −0.10 ± 0.23 | 173, 174, 175, 176, 177 |
| 110 | 0.00 ± 0.40 | −0.11 ± 0.46 | −0.08 ± 0.33 | 178, 179 |
| **111** | **−0.18 ± 0.35** | **0.21 ± 0.46** | **0.15 ± 0.32** | **180** |
| **112** | **−0.30 ± 0.32** | **−0.24 ± 0.41** | **−0.17 ± 0.29** | **181** |
| **113** | **−0.29 ± 0.33** | **−0.06 ± 0.45** | **−0.04 ± 0.32** | **182** |
| 114 | −0.16 ± 0.25 | 0.07 ± 0.34 | 0.05 ± 0.24 | 183, 184, 185, 186 |
| 115 | −0.07 ± 0.26 | 0.01 ± 0.37 | 0.01 ± 0.26 | 187, 188, 189, 190, 191 |
| 116 | 0.09 ± 0.25 | −0.17 ± 0.37 | −0.12 ± 0.26 | 192, 193, 194 |
| 117 | −0.10 ± 0.25 | −0.06 ± 0.37 | −0.04 ± 0.26 | 195, 196, 197, 198 |
| 118 | 0.13 ± 0.32 | 0.32 ± 0.42 | 0.23 ± 0.29 | 199 |
| 119 | −0.13 ± 0.29 | −0.06 ± 0.37 | −0.04 ± 0.26 | 200, 201, 202 |
| 120 | −0.40 ± 0.29 | −0.26 ± 0.44 | −0.18 ± 0.31 | 203 |
| 121 | 0.19 ± 0.29 | 0.37 ± 0.39 | 0.26 ± 0.28 | 204 |
| 122 | −0.49 ± 0.29 | 0.01 ± 0.38 | 0.01 ± 0.27 | 205 |
| 123 | 0.38 ± 0.23 | −0.03 ± 0.35 | −0.02 ± 0.25 | 206, 207, 208, 209, 210 |
| 124 | −0.71 ± 0.29 | −0.35 ± 0.38 | −0.25 ± 0.27 | 212 |
| 125 | −0.01 ± 0.20 | 0.70 ± 0.32 | 0.49 ± 0.23 | 213 |
| 126 | 0.16 ± 0.30 | −0.10 ± 0.41 | −0.07 ± 0.29 | 214 |
| 127 | 0.10 ± 0.32 | 0.30 ± 0.34 | 0.22 ± 0.24 | 216 |
| 128 | 0.04 ± 0.30 | 0.89 ± 0.23 | 0.63 ± 0.17 | 217 |
| 129 | −0.60 ± 0.30 | 0.07 ± 0.61 | 0.01 ± 0.11 | 218 |

[a]Faults that bound blocks that have no GPS stations on them are bold.

than 1°/My with a few exceptions (Table 3). The estimated uncertainties in the block rotation rates are generally small (below 0.2°/My in most cases), but are derived under the assumption that the blocks are rigid and that the boundaries we have drawn for them are correct. In over half the blocks the vertical axis spin rates are lower than the uncertainties.

[40] The most rapidly rotating block in our model is the Carson Domain (Figures 8 and 10b). Paleomagnetism of this block was measured by *Cashman and Fontaine* [2000], who found a rotation rate of 2.8 to 5.7°/My over the last 9–13 My. While our model shows a sign of rotation and interaction with other blocks that are similar to their model, our estimate of 1.3 ± 0.1°/My clockwise is significantly smaller. The velocity gradients (1.9 mm/yr over the 50 km width of the block) could be partially explained by deformation within the Carson domain. There is geologic evidence for faulting within and near the perimeter of this block, especially in oroclinal folding near its eastern edge

**Table 3.** Block Rotation and Spin Rates

| Block[a] | $N$[b] | Latitude | Longitude | Correlation[c] | Rotation Rate (°/My) | Spin Rate[d] (°/My) |
|---|---|---|---|---|---|---|
| 1[e] | 19 | −23.4 ± 0.0 | −161.6 ± 0.0 | 0.062 | 0.110 ± 0.000 | 0.032 ± 0.000 |
| 2 | 17 | −51.6 ± 7.4 | 76.4 ± 12.0 | 0.412 | 0.280 ± 0.059 | −0.269 ± 0.057 |
| 3 | 2 | −52.1 ± 23.9 | 77.3 ± 39.9 | 0.395 | 0.234 ± 0.163 | −0.223 ± 0.157 |
| 4 | 5 | −47.6 ± 263.0 | 174.8 ± 139.8 | −0.070 | 0.064 ± 0.163 | −0.016 ± 0.187 |
| 5 | 0 | −60.1 ± 87.4 | 115.9 ± 79.9 | −0.597 | 0.143 ± 0.201 | −0.109 ± 0.198 |
| 6 | 1 | −56.7 ± 36.6 | 98.8 ± 60.3 | −0.336 | 0.196 ± 0.201 | −0.168 ± 0.195 |
| 7 | 2 | 0.2 ± 77.6 | −149.6 ± 80.7 | −0.002 | 0.140 ± 0.153 | 0.095 ± 0.198 |
| 8 | 3 | −43.2 ± 7.0 | 65.0 ± 9.6 | 0.472 | 0.916 ± 0.155 | −0.912 ± 0.152 |
| 9 | 6 | −42.6 ± 6.7 | 63.7 ± 9.0 | 0.465 | 1.124 ± 0.177 | −1.121 ± 0.174 |
| 10 | 2 | −52.3 ± 27.7 | 80.6 ± 50.5 | 0.333 | 0.222 ± 0.194 | −0.210 ± 0.187 |
| 11 | 2 | −57.8 ± 42.7 | 98.2 ± 69.9 | −0.322 | 0.168 ± 0.200 | −0.144 ± 0.194 |
| 12 | 1 | −55.2 ± 186.9 | 152.9 ± 90.5 | −0.404 | 0.101 ± 0.177 | −0.049 ± 0.191 |
| 13 | 4 | −54.3 ± 28.3 | 87.1 ± 55.9 | 0.125 | 0.206 ± 0.197 | −0.189 ± 0.191 |
| 14 | 5 | −44.4 ± 11.7 | 67.1 ± 16.7 | 0.478 | 0.598 ± 0.175 | −0.593 ± 0.171 |
| 15 | 6 | −41.8 ± 3.7 | 63.2 ± 4.9 | 0.465 | 1.259 ± 0.109 | −1.257 ± 0.108 |
| 16 | 3 | −45.0 ± 13.1 | 67.0 ± 18.6 | 0.476 | 0.529 ± 0.173 | −0.525 ± 0.169 |
| 17 | 1 | 13.1 ± 58.1 | −141.0 ± 66.7 | −0.122 | 0.128 ± 0.124 | 0.108 ± 0.147 |
| 18 | 3 | −50.0 ± 266.8 | 166.3 ± 135.9 | −0.195 | 0.065 ± 0.166 | −0.023 ± 0.186 |
| 19 | 0 | 6.3 ± 108.0 | −143.6 ± 123.9 | −0.056 | 0.087 ± 0.148 | 0.067 ± 0.184 |
| 20 | 0 | −54.1 ± 319.3 | 162.8 ± 148.1 | −0.263 | 0.062 ± 0.182 | −0.026 ± 0.197 |
| 21 | 1 | −55.2 ± 371.3 | 163.0 ± 165.5 | −0.266 | 0.056 ± 0.187 | −0.024 ± 0.201 |
| 22 | 4 | −47.1 ± 22.7 | 69.3 ± 33.6 | 0.480 | 0.309 ± 0.182 | −0.305 ± 0.177 |
| 23 | 4 | −43.9 ± 11.3 | 66.9 ± 16.1 | 0.482 | 0.606 ± 0.172 | −0.602 ± 0.168 |
| 24 | 4 | −46.0 ± 14.2 | 69.0 ± 20.9 | 0.483 | 0.438 ± 0.161 | −0.433 ± 0.157 |
| 25 | 3 | −23.2 ± 157.1 | −166.4 ± 127.5 | 0.090 | 0.083 ± 0.139 | 0.020 ± 0.195 |
| 26 | 7 | −49.0 ± 18.1 | 76.4 ± 31.6 | 0.426 | 0.261 ± 0.144 | −0.252 ± 0.139 |
| 27 | 2 | −56.1 ± 77.3 | 111.2 ± 91.2 | −0.568 | 0.114 ± 0.179 | −0.091 ± 0.177 |
| 28 | 4 | −54.1 ± 21.2 | 89.0 ± 43.7 | 0.044 | 0.146 ± 0.109 | −0.133 ± 0.106 |
| 29 | 2 | −44.1 ± 10.1 | 66.4 ± 14.2 | 0.485 | 0.568 ± 0.142 | −0.565 ± 0.139 |
| 30 | 1 | −38.6 ± 192.1 | −174.8 ± 117.7 | 0.062 | 0.059 ± 0.110 | −0.003 ± 0.141 |
| 31 | 4 | −47.5 ± 11.8 | 73.5 ± 19.3 | 0.466 | 0.261 ± 0.088 | −0.255 ± 0.086 |
| 32 | 7 | −43.3 ± 8.8 | 63.9 ± 11.9 | 0.478 | 0.695 ± 0.145 | −0.693 ± 0.143 |
| 33 | 0 | −58.4 ± 460.6 | 164.0 ± 180.9 | −0.271 | 0.049 ± 0.192 | −0.023 ± 0.203 |
| 34 | 2 | −47.2 ± 25.7 | 68.7 ± 37.3 | 0.494 | 0.267 ± 0.175 | −0.264 ± 0.171 |
| 35 | 7 | −43.9 ± 11.5 | 65.4 ± 16.2 | 0.484 | 0.479 ± 0.136 | −0.478 ± 0.134 |
| 36 | 3 | −46.9 ± 23.5 | 68.7 ± 34.5 | 0.504 | 0.258 ± 0.156 | −0.256 ± 0.153 |
| 37 | 3 | −51.3 ± 36.3 | 74.5 ± 57.8 | 0.466 | 0.192 ± 0.194 | −0.185 ± 0.187 |
| 38 | 5 | −50.6 ± 31.4 | 75.7 ± 52.6 | 0.446 | 0.174 ± 0.159 | −0.168 ± 0.154 |
| 39 | 1 | −49.3 ± 24.7 | 73.2 ± 39.5 | 0.477 | 0.198 ± 0.137 | −0.193 ± 0.133 |
| 40 | 1 | −55.0 ± 35.3 | 83.0 ± 66.7 | 0.294 | 0.120 ± 0.138 | −0.112 ± 0.133 |
| 41 | 4 | −56.0 ± 38.6 | 87.6 ± 75.7 | 0.108 | 0.112 ± 0.145 | −0.102 ± 0.140 |
| 42 | 10 | −45.7 ± 10.7 | 67.8 ± 15.5 | 0.502 | 0.308 ± 0.084 | −0.305 ± 0.082 |
| 43 | 2 | −62.6 ± 119.1 | 99.9 ± 174.0 | −0.428 | 0.067 ± 0.201 | −0.057 ± 0.195 |
| 44 | 2 | 15.6 ± 94.6 | −135.6 ± 112.3 | −0.169 | 0.093 ± 0.163 | 0.082 ± 0.185 |
| 45 | 5 | −47.5 ± 21.0 | 70.1 ± 31.8 | 0.505 | 0.230 ± 0.128 | −0.227 ± 0.125 |
| 46 | 2 | −48.1 ± 24.9 | 73.7 ± 40.9 | 0.469 | 0.199 ± 0.142 | −0.194 ± 0.138 |
| 47 | 1 | −50.0 ± 32.7 | 74.9 ± 54.5 | 0.474 | 0.174 ± 0.165 | −0.168 ± 0.160 |
| 48 | 4 | −49.0 ± 27.5 | 73.0 ± 43.9 | 0.495 | 0.193 ± 0.147 | −0.188 ± 0.144 |
| 49 | 1 | −46.6 ± 14.2 | 69.0 ± 21.1 | 0.509 | 0.266 ± 0.098 | −0.263 ± 0.096 |
| 50 | 2 | −55.5 ± 557.5 | 175.0 ± 217.8 | −0.091 | 0.039 ± 0.180 | −0.014 ± 0.201 |
| 51 | 0 | −59.8 ± 568.5 | 167.8 ± 195.1 | −0.235 | 0.042 ± 0.184 | −0.019 ± 0.199 |
| 52 | 4 | −23.3 ± 225.9 | −149.0 ± 214.5 | 0.193 | 0.038 ± 0.116 | 0.013 ± 0.148 |
| 53 | 4 | −45.4 ± 15.9 | 68.9 ± 24.0 | 0.513 | 0.282 ± 0.119 | −0.279 ± 0.117 |
| 54 | 4 | −49.8 ± 34.2 | 75.0 ± 57.8 | 0.482 | 0.164 ± 0.165 | −0.159 ± 0.161 |
| 55 | 3 | −56.6 ± 52.8 | 89.8 ± 106.9 | 0.011 | 0.096 ± 0.174 | −0.087 ± 0.170 |
| 56 | 3 | −17.1 ± 239.2 | −148.3 ± 237.2 | 0.145 | 0.045 ± 0.148 | 0.020 ± 0.190 |
| 57 | 3 | −66.8 ± 153.5 | 111.3 ± 131.3 | −0.653 | 0.059 ± 0.134 | −0.046 ± 0.133 |
| 58 | 3 | −53.6 ± 36.9 | 79.8 ± 68.2 | 0.406 | 0.117 ± 0.138 | −0.111 ± 0.134 |
| 59 | 3 | −47.5 ± 28.5 | 70.9 ± 44.0 | 0.520 | 0.215 ± 0.165 | −0.211 ± 0.162 |
| 60 | 4 | −23.9 ± 157.5 | −163.9 ± 134.4 | 0.102 | 0.075 ± 0.134 | 0.019 ± 0.182 |

[a]Block number refers to annotation in Figure 8b.
[b]$N$ is number of GPS sites on this block.
[c]Correlation between latitude and longitude estimates.
[d]Counterclockwise vertical axis rotation rates are positive.
[e]Block 1 (SNGV) has zero uncertainty because its rotation is fixed in the inversion.

[*Faulds and Ramelli*, 2005; *Faulds and Henry*, 2008], and the large coherent blocks of *Cashman and Fontaine* [2000] may not be supported by these more recent observations. In our model, residual velocities for the 6 GPS sites on this block have RMS misfit of 0.4 mm/yr (about average for the entire model) and appear random. However, it is possible we are interpreting a combination of rotation and shear as purely rigid rotation. If this is the case then the true con-

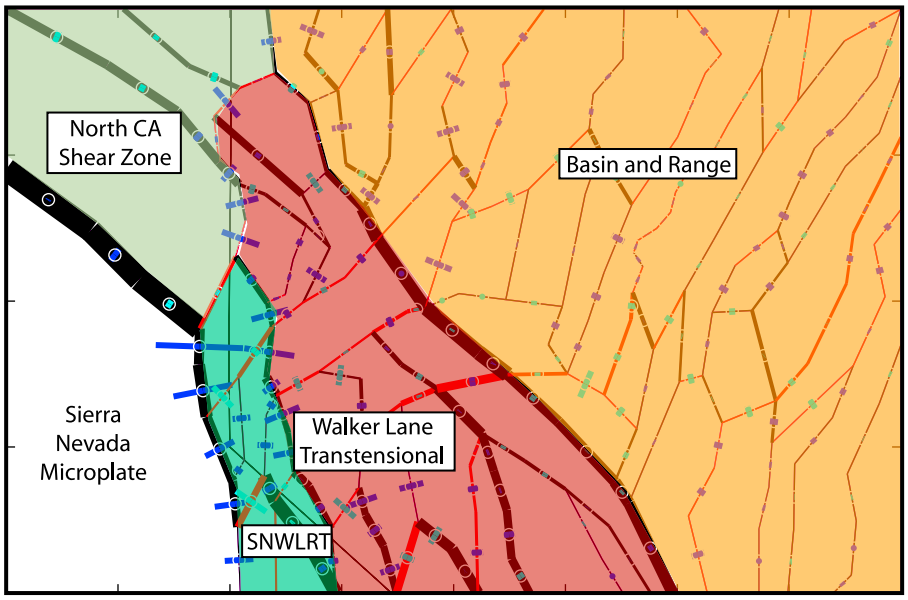


**Figure 12.** Domains of crustal deformation distinguished by the rates, patterns, and styles of deformation, discussed in the text. SNWLT, Sierra Nevada/Walker Lane transition.

temporary rotation rate would be even lower than we have estimated, increasing the difference between the past and present-day rotation rate. Relaxing the model regularization parameters, as in Figure 10c, does not increase the rotation rate for this block, so the rotation rate is not sensitive to model regularization.

[41] The difference between the geodetic and paleomagnetic measurements could indicate that rotation rates of this domain have decreased over time, and that as the Walker Lane continues to develop structurally, the role of faulting is increasing while the role of block rotations is decreasing. It is expected from simple models of crustal blocks rotating in a wide shear zone that their vertical axis spin rate will vary over time, especially when the blocks vary in their size, orientation and pattern of arrangement [*Lamb*, 1994]. Also there is a trade-off between rotations and faulting for blocks inside a shear zone, so that the balance of one regime over another may reflect the source of stress in the deforming zone [*McCaffrey*, 2005]. Thus, the evolution of the system could be a reflection of a change in driving stress, e.g., from a change in SNGV motion relative to the Basin and Range around 8–10 Ma [*Wernicke and Snow*, 1998]. Alternatively, the change could be a more gradual evolution that is a natural response of faults to provide less resistance to deformation as cumulative slip on the faults increases [e.g., *Parsons*, 2002].

[42] In another case, along the Honey Lake, Warm Springs dextral strike-slip faults, paleomagnetic observations indicate a small degree (~15°) counterclockwise rotation of blocks wedged between the left steps of en echelon dextral faults [*Faulds et al.*, 2005]. In their model, these Riedel shears rotate counterclockwise to better align themselves to accommodate regional shear deformation, possibly in the process of developing a throughgoing lithospheric-scale dextral fault. These rotations would likely slow down over time as the faults become better aligned to accommodate the regional shear deformation. Our GPS stations are spaced too far apart to resolve the reported CCW rotation, and even if we had very dense observations the elastic strain accumulation we measure might not reveal detailed strain release patterns such observed between en echelon faults. Nonetheless, these rotations may occur and may be an example of rotations that are changing rate over time and giving way to more energetically efficient faulting patterns in the NWL.

### 4.3. Comparison of Geologic and Geodetic Measures of Deformation

[43] We compare the results of our geodetically constrained block model to rates from various published studies of NWL fault slip rates (Table 4). Figure 14 shows the relationship between the rates, compared to a diagonal line of slope one that indicates where perfect agreement would occur. Geodetic slip rate uncertainties are taken from Table 2. Uncertainties in geologic rates are those from the published studies and are one-sided where a minima or maxima were reported. Where multiple rates were available in the literature (e.g., for the Honey Lake fault) a value consistent with all studies was used when possible. For the Honey Lake fault, ranges of values in separate studies varied from 1.1 to 2.6 mm/yr (Table 4). We chose a single representative value of $1.8 \pm 0.35$ since this value lies in the middle of the range of the Quaternary studies and the 95% confidence interval of this uncertainty spans the range of values. The rates estimated from the offset paleovalleys of *Faulds et al.* [2005] and *Hinz et al.* [2009] include offsets from the Pyramid Lake fault, and hence were not used in the direct comparison in Figure 14.

[44] We find that out of 12 slip rate estimates there are 10 which have error bars that cross the diagonal line (although just barely for the Honey Lake fault) indicating an agreement between the geologic and geodetic rates to within uncertainty. For the rates that disagree there may be specific reasons for the misfit that are attributable to our block modeling methodology. For example, the Benton Springs

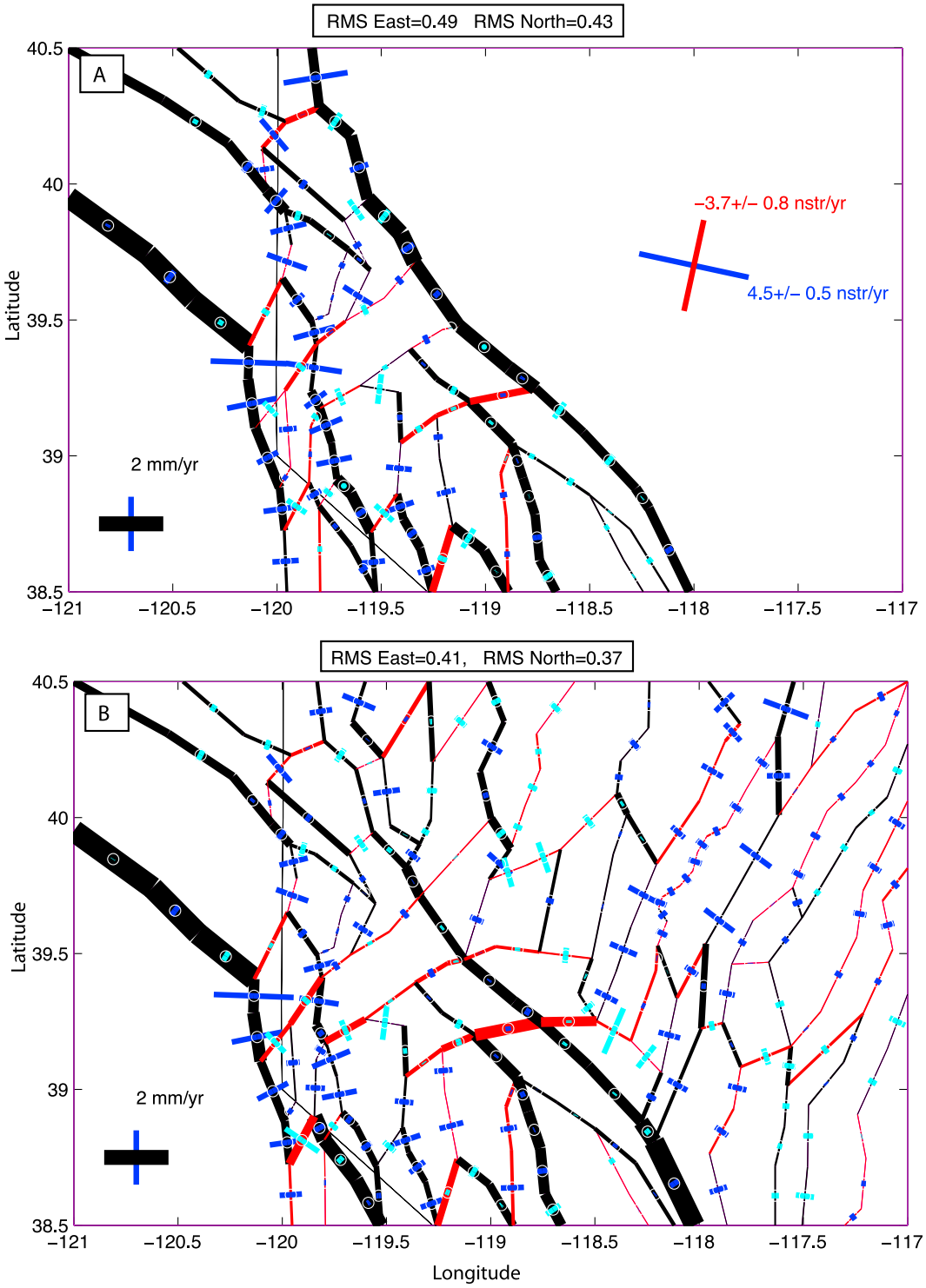


**Figure 13.** (a) Same as Figure 10 except that block model has 29 blocks where Basin and Range domain has been greatly simplified into a single block that experiences rotation and horizontal tensor strain. (b) Same as Figure 10 except that velocities are not corrected for postseismic relaxation owing to CNSB historic earthquakes. Slip rate indicators are the same as in Figure 10.

geologic rate is higher than the geodetic rate. However, Petrified Springs has a higher geodetic rate. Thus it may be that the design of the block model is favoring slip on the Petrified Springs fault, e.g., by having a better aligned connection to faults to the north. The Benton Springs and Petrified Springs together add up to 2.0 mm/yr geodetic, and 2.1 mm/yr geologic, and thus have a compatible slip budget as a collaborative system. In other cases, some geologic rates may agree with a given geodetic slip rate, while others do not. For example, *Hinz et al.* [2009] report a slip rate for

**Table 4.** Northern Walker Lane, Basin and Range Published Geologic Slip Rates

| Fault Name | Reference | Constraint Type | Over Period (ybp) | Slip Rate (mm/yr) | Type |
|---|---|---|---|---|---|
| Dixie Valley | *Bell et al.* [2004] | trench/dating | 12000 | 0.71/0.55[a] | Normal |
| Rainbow Mtn | *Bell et al.* [2004] | trench/dating | 14500 | 0.23 | Max. Normal |
| Fourmile Flat | *Bell et al.* [2004] | trench/dating | 8800 | 0.36 | Max. Normal |
| Fairview Pk. | *Bell et al.* [2004] | trench/dating | 35400 | 0.21 | Max. Normal |
| Sand Springs | *Bell et al.* [2004] | trench/dating | 13300 | 0.5 | Max. Normal |
| Honey Lake, Warm Springs, Pyramid System | *Faulds et al.* [2005] | offset paleovalleys | 9 to 3 million | 2.2 to 10.0 | Range Dextral |
| Honey Lake | *Hinz et al.* [2009] | offset paleovalleys | 6 to 3 million | 3.3 to 10.0 | Range Dextral |
| Honey Lake | *Turner et al.* [2008] | trenching | | 1.7 | Dextral |
| Honey Lake | *Wills and Borchardt* [1993] | trenching | Holocene | 1.1 to 2.6 | Range Dextral |
| Pyramid Lake | *Briggs and Wesnousky* [2004] | mapping | Late Pleistocene to Holocene | 2.6 | Dextral |
| Genoa | *Ramelli et al.* [1999] | trenching | Holocene | 2.5 | Normal |
| West Tahoe | *Kent et al.* [2005] | offset geologic markers | 19200 | 0.57[b] | Normal |
| Stateline | *Kent et al.* [2005] | | 19200 | 0.46[b] | Normal |
| Mohawk Valley | *Sawyer et al.* [2005] | trenching | Holocene | 0.3 | Min. Dextral |
| Petrified Springs | *Wesnousky* [2005a] | offset geomorph. | Quaternary | 1.1 | Min. Dextral |
| Benton Springs | *Wesnousky* [2005a] | offset geomorph. | Quaternary | 1.0 | Min. Dextral |

[a]Negative slip rate is normal or dextral based on alternative dips of 45° and 65°.
[b]Negative slip rate is normal or dextral based on 60° dips assumed by *Kent et al.* [2005].

the Honey Lake fault of 1.7–2.8 mm/yr for a 6 Ma initiation of slip, and 3.3–5.7 mm/yr for a 3 Ma initiation. Our geodetic value of 1.2 ± 0.3 mm/yr is more consistent with the 6 Ma initiation values and in that case is consistent to within uncertainties. Thus we speculate that the geodetic rates may help resolve an ambiguity in the timing of initiation of slip on the Honey Lake fault. Our geodetic value is also consistent with the lower end of the ranges provided by *Wills and Borchardt* [1993] and *Turner et al.* [2008].

[45] The other fault for which there is a significant disagreement is the Genoa fault, where the geologic rate (2–3 mm/yr) is significantly greater than the geodetic rate

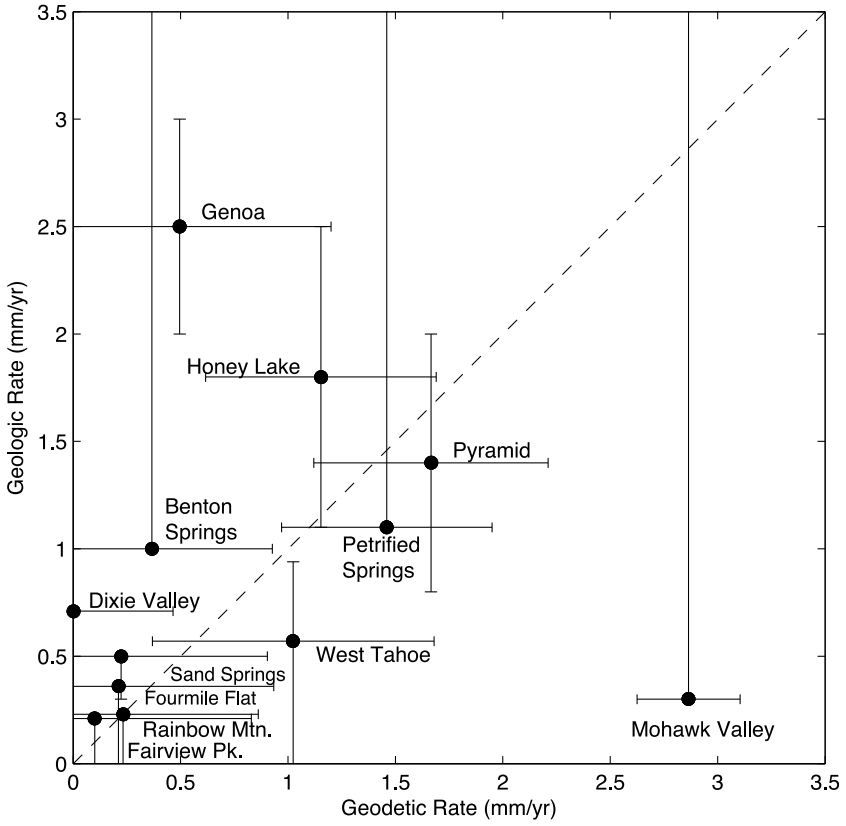


**Figure 14.** Comparison between geologic slip rates and slip rates obtained in model shown in Figure 10. Diagonal dashed line indicates where geologic and geodetic slip rates are equal. Names of faults are given and error bars are 2 $\sigma$ for geologic rates, and sometimes one sided for geodetic rates. See text for discussion.

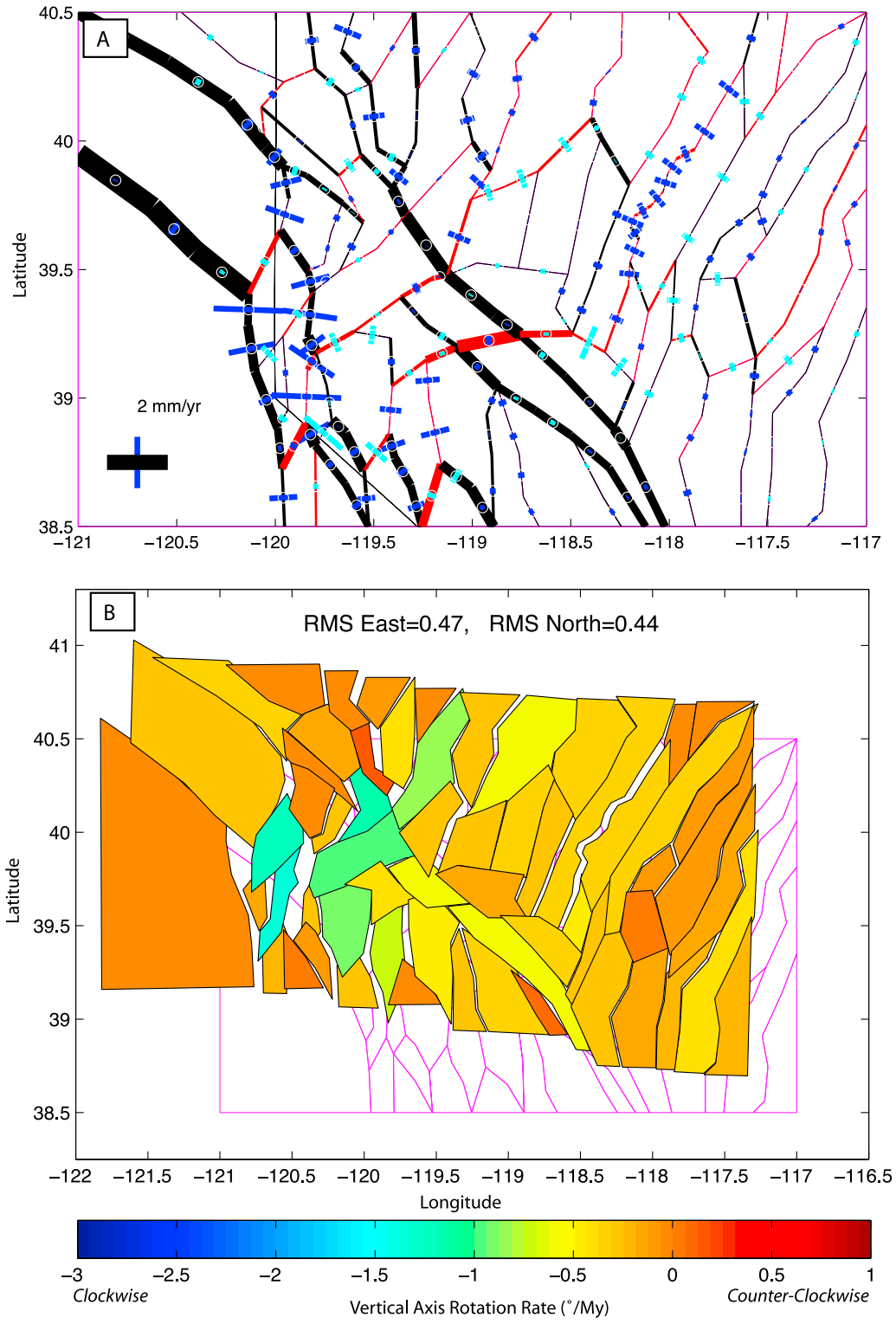


**Figure 15.** Same as Figure 10 except that geologic slip rates from Table 4 are additionally applied as constraints on the block motions. Note that Mohawk Valley geologic slip rate has been omitted.

(0.3 ± 0.3 mm/yr horizontal extension normal to the fault). Our geodetic rate may be too low because of lack of constraint on the Tahoe block immediately to the west of the Carson Range, and also because our model geometry that may be simplified compared to the real complexity of the Tahoe/Sierra/Basin and Range transition, which is a small fraction of our modeling domain. Testing a model where the Tahoe and Carson Range blocks are combined assumes that slip on the east Lake Tahoe fault is zero (for which evidence of recent slip is equivocal [*U.S. Geological*

*Survey and Nevada Bureau of Mines and Geology*, 2006]) only increases the normal slip rate on the Genoa to 0.4 mm/yr. This area has the highest strain rates in the NWL, and so a detailed study is likely required to resolve whether the difference between geological and geodetic rates is real.

[46] In order to determine if a self-consistent model can be constructed that satisfies both geologic and geodetic constraints, we have constructed a model that includes geologic slip rates as constraints in the inversion (Figure 15). One geologic estimate, that of the Mohawk Valley fault is 0.3 mm/yr [*Sawyer et al.*, 2005], and is much lower than the geodetic rate 2.9 ± 0.1 mm/yr. However, this geologic rate was expressed as a minimum and hence is technically in agreement with our estimate. We omit the Mohawk Valley slip rate because using 0.3 mm/yr results in a profound distortion of the pattern of block motions, with a much higher misfit to geodetic data. The integrated GPS and geologic model fits the GPS data slightly worse than the GPS-only model, with RMS residual velocity of 0.47 east (0.44 west) mm/yr. The biggest changes in the model occur where there are differences between geodetic and geologic slip rates. For example the increased normal extension rate on the Genoa fault can be seen in the increased space generated between the block 8:Carson Range and block 11:Carson Valley in Figure 15b compared to Figure 10b. Thus the disagreements cause minor changes in the regional pattern of block motions, but do not change the slip styles on faults or the region organization of block motions. The similarity between this model and the GPS-only model suggests that GPS slip rate estimates are similar to geologic rates, and that the geologic rates tend to be consistent with the far-field budgets even though geologic rates are insufficient in number to add up to the far-field motions.

### 4.4. Effect of Postseismic Relaxation

[47] Several lines of evidence suggest that CNSB postseismic relaxation causes a significant distortion of the geodetic velocity field that is not representative of long-term deformation. These arguments include (1) the presence of anomalously high rates of geodetically observed dilatation [*Svarc et al.*, 2002; *Hammond and Thatcher*, 2004], (2) vertical motions inferred from InSAR and GPS whose patterns are consistent with viscoelastic relaxation models [*Gourmelen and Amelung*, 2005], (3) better agreement between geologic and geodetic slip rates after the correction is applied [*Bell et al.*, 2004; *Hammond et al.*, 2009], (4) better agreement between strain rates in the Basin and Range domain and in eastern Nevada [*Hammond et al.*, 2011] after the correction is applied, and (5) viscoelastic behavior that has been observed after other more recent earthquakes in the western United States where better observations were possible, e.g., the Landers and Hector Mine earthquakes [e.g., *Pollitz et al.*, 2000]. Nonetheless it could still be possible that instead the CNSB area is a region of anomalously high slip rates that persists over a least several seismic cycles. This is suggested by a compilation of paleoseismic studies across the NWL [*Wesnousky et al.*, 2005], and similar to the higher rates of dextral slip we infer at the eastern edge of the NWL.

[48] However, one further argument suggests that viscoelastic relaxation biases slip rates in the uncorrected model. The effect of the correction is illustrated by estimating the block motions using the velocity field without the correction applied. In the uncorrected model (Figure 13b), normal slip rates across faults are larger in the vicinity of the CNSB epicenters, where the viscoelastic model has the largest velocity gradients. Thus the correction most strongly affects deformation in the Basin and Range domain (Figure 12), in a zone about 3 ranges wide, that includes Dixie Valley, the Stillwater Range, Edwards Creek Valley and the Clan Alpine Range. The uncorrected horizontal extension rates on 5 parallel fault systems across the CNSB (trains 89, 92, 100, 108, 112; Table 2) sums to 2.2 mm/yr, which is reduced to 0.5 mm/yr when the correction is applied. Aside from the uniformity of the corrected model, discrepancies between geologic rates argue for the need for the correction. For example, the Clan Alpine fault had three events in the last 130 ka [*Machette et al.*, 2002], which imply with the uncorrected slip rate of 0.3 mm/yr a per event slip of ~13 m. However, if the corrected slip rate is used (0.1 mm/yr) then the per event slip is inferred to be ~4 m, which is in better agreement to observed per event offset for most paleoearthquakes and historic earthquakes.

## 5. Conclusions

[49] We have estimated rates of crustal motion from GPS data obtained in the Mobile Array of GPS for Nevada Transtension (MAGNET) and other regional continuous GPS networks including the EarthScope Plate Boundary Observatory. We present 224 new velocities with an average station spacing of ~20 km and a median uncertainty of 0.3 mm/yr. The velocity field illustrates the potential for using the semicontinuous GPS observation strategy in resolving deformation patterns in regions of complex crustal deformation.

[50] We have estimated fault slip rates by applying a block modeling methodology that solves for block rotations. The velocity field has been corrected for viscoelastic postseismic relaxation from 20th century earthquakes in the Central Nevada Seismic Belt. Slip rates estimated by GPS geodesy are in agreement with geologic slip rates, to within uncertainties, in 10 out of 12 cases where both numbers are well constrained. This suggests that smaller blocks of crust tend to move with a steady secular motion, similar to that observed for larger plates and major plate boundary faults.

[51] Rotation rates for the Carson Domain are 1.3 ± 0.1°/My clockwise, significantly lower, but in the same direction as those obtained from paleomagnetic measurements. This suggests that its rotation rate may be decreasing over time, and that the role of faulting has been increasing while the role of block rotations has been decreasing in the NWL over the past 9–13 My.

## Appendix A

[52] The detailed expressions for our block modeling method are provided by *Hammond and Thatcher* [2007]. We extend the method to additionally solve for a constant horizontal tensor strain rate in each block (when desired), and to regularize the solution by including a damping constraint on vertical axis rotation rates. We summarize the relationships here to place our new features into context.

[53] The long-term velocity averaged over many seismic cycles is equal to the sum of the interseismic and coseismic velocities

$$v_{LongTerm} = v_{Interseismic} + v_{Coseismic} \tag{A1}$$

rearranging gives

$$v_{Interseismic} = v_{LongTerm} - v_{Coseismic} \tag{A2}$$

which is the relationship between the GPS velocities, block motion and fault slip. This implements the back slip approach introduced by *Savage* [1983]. Coseismic velocity is defined as the rate of movement of a point near the fault associated with coseismic offsets averaged over many seismic cycles. We parameterize block motion with Euler rotations and slip with

$$v_{GPS,i} = \omega_j \times r_i - \sum_{k=1}^{L} \left(a_k G_{ss,ki} + b_k G_{N,ki}\right) \tag{A3}$$

where $\boldsymbol{\omega}_j$ is an unknown block rotation vector of block $j$. The strike slip $a_k$ and dip slip $b_k$ rates are unknowns that scale the unit slip functions $\boldsymbol{G}_{SS}$ and $\boldsymbol{G}_N$ that represent the pattern of strike slip and normal slip, respectively, for each fault segment $k$. These functions are calculated for each fault segment using the functions of *Okada* [1985], since the dip, length, and width of the fault are predefined. Positive unit slip is sinistral for $a_k$ and in the thrust sense for $b_k$. Since GPS sites can be affected by elastic strain accumulation on more than one fault segment, especially in complex zones with densely spaced faults, this term is summed over the nearest $L$ fault segments.

[54] We add model parameters for horizontal tensor strain rate and take the dot product with the north $e_N$ and east $e_E$ unit vectors to obtain separate equations for each component

$$v_{N,i} = \left[\omega_i \times r_i - \sum_{k=1}^{L} \left(a_k G_{SS,ki} + b_k G_{N,ki}\right)\right] \bullet e_N - \varepsilon_{\phi\theta} r_0 \sin\theta_0 \Delta\phi - \varepsilon_{\theta\theta} r_0 \Delta\theta \tag{A4}$$

$$v_{E,i} = \left[\omega_i \times r_i - \sum_{k=1}^{L} \left(a_k G_{SS,ki} + b_k G_{N,ki}\right)\right] \bullet e_E - \varepsilon_{\phi\phi} r_0 \sin\theta_0 \Delta\phi - \varepsilon_{\theta\phi} r_0 \Delta\theta \tag{A5}$$

where $\varepsilon_{\varphi\varphi}$, $\varepsilon_{\theta\theta}$, and $\varepsilon_{\theta\varphi}$ are the three strain rate free parameters, expressed in colatitude $\theta$ and longitude $\varphi$ following *Savage et al.* [2001], $r_0$ is the radius of the Earth, $\Delta\theta$ and $\Delta\varphi$ are the angles from the center of the block to the site.

[55] We regularize the inversion by applying three types of constraints which are additional equations that must be satisfied in the inversion. The first condition is the consistency between relative block motions and slip rates. This condition provides two additional equations for each fault segment because it is evaluated at the mid point of each fault segment for both components of slip [*Hammond and Thatcher*, 2007]. In all models this condition is assigned a very strong weight in the inversion, with a prior uncertainty $\alpha$ of $10^{-6}$ m/yr (Table 1), since it is fundamental to the estimation of slip rates from relative block motions.

[56] The second condition is that vertical axis rotations, i.e., spin rates, must be minimized. Equations (A4) and (A5) solve for Euler rotation vectors which amount to spin-free translation when the angle between $\boldsymbol{r}_i$ and $\boldsymbol{\omega}_i$ is 90°. We set the condition that

$$\omega_j \bullet r_j = 0 \tag{A6}$$

for each block $j$. When the prior uncertainty of $\beta$ is very small, the vertical axis rotation rates are forced to be zero, restricting to solution to one where blocks only translate but do not spin. When this condition is relaxed by using larger values of $\beta$, vertical axis rotations are minimized subject to the other constraints, e.g., that the data be fit.

[57] The third condition is that both components of the fault slip rates are minimized. This condition is applied by adding the additional equations $a_k = 0$ and $b_k = 0$ for each fault. A very small value for the prior uncertainty of these constraints $\gamma$ results in a model with no relative motion of blocks since slip rates are connected to block motions through slip rate consistency.

[58] For the NWL we identify $\beta$ and $\gamma$ values that strike a balance between minimizing misfit to the data, and minimizing slip rates and spin rates. We iterate through trial values of these parameters, solving for the model, and evaluating misfit and parameter norms. For $\gamma$ we iterate through values between $10^{-6}$ to 1 m/yr, and calculate the $\chi^2$ per degree of freedom misfit and the norm of the model slip rates vector (Figure 9b). For $\beta$ we iterate through values between $10^{-12}$ to $10^{-18}$/yr, and calculate $\chi^2$ and the norm of the model spin rates (Figure 9c). For our preferred model (Figures 10a and 10b) we chose values that provide both low misfit and low model norm (Table 1).

[59] **Acknowledgments.** This work was made possible by support from the NSF Tectonics program and NV EPSCoR program under project 0610031, NSF EarthScope project 0635757, and USGS NEHRP awards 07HQGR0027 and 08HQGR0027. Essential support has also been provided by UNAVCO, Inc. for the deployment of PBO and archiving of EarthScope data, by the International GNSS Service for continuous GPS station data archiving and support, and by the original developers of the BARGEN and BARD networks. Data were also provided by Washoe county, Nevada. The Jet Propulsion Laboratory provides the GIPSY software and GPS products. We thank Alpine Meadows and the U.C. Berkeley Sagehen Research Field Station for hosting GPS sites. Bret Pecoraro provided backbone GPS field support for MAGNET. Fieldwork was also contributed by Hans-Peter Plag, Sumant Jha, Xiaohui Zhou, and Jayne Bormann. This manuscript improved substantially from reviews by Rob McCaffrey, Jim Faulds, and an anonymous reviewer.

## References

Agnew, D. C. (1992), The time-domain behavior of power law noises, *Geophys. Res. Lett.*, *19*, 333–336, doi:10.1029/91GL02832.

Argus, D. F., and R. G. Gordon (1991), Current Sierra Nevada-North America motion from very long baseline interferometry: Implications for the kinematics of the western United States, *Geology*, *19*, 1085–1088, doi:10.1130/0091-7613(1991)019<1085:CSNNAM>2.3.CO;2.

Bell, J. W., C. M. dePolo, A. R. Ramelli, A. M. Sarna-Wojcicki, and C. E. Meyer (1999), Surface faulting and paleoseismic history of the 1932 Cedar Mountain earthquake area, west-central Nevada, and implications for modern tectonics of the Walker Lane, *Geol. Soc. Am. Bull.*, *111*(6), 791–807, doi:10.1130/0016-7606(1999)111<0791:SFAPHO>2.3.CO;2.

Bell, J. W., S. J. Caskey, A. R. Ramelli, and L. Guerrieri (2004), Pattern and rates of faulting in the Central Nevada Seismic Belt, and paleoseismic evidence for prior belt-like behavior, *Bull. Seismol. Soc. Am.*, *94*, 1229–1254, doi:10.1785/012003226.

Bennett, R. A., W. Rodi, and R. E. Reilinger (1996), Global Positioning System constraints on fault slip rates in southern California and northern

Baja, Mexico, *J. Geophys. Res.*, *101*, 21,943–21,960, doi:10.1029/96JB02488.

Bennett, R. A., B. P. Wernicke, N. A. Niemi, A. M. Friedrich, and J. L. Davis (2003), Contemporary strain rates in the northern Basin and Range province from GPS data, *Tectonics*, *22*(2), 1008, doi:10.1029/2001TC001355.

Bird, P. (2007), Uncertainties in long-term geologic offset rates of faults: General principles illustrated with data from California and other western states, *Geosphere*, *3*(6), 577–595, doi:10.1130/GES00127.1.

Blewitt, G. (2008), Fixed-point theorems of GPS carrier phase ambiguity resolution and their application to massive network processing: Ambizap, *J. Geophys. Res.*, *113*, B12410, doi:10.1029/2008JB005736.

Blewitt, G., et al. (2005), A stable North America reference frame (SNARF): First release, paper presented at UNAVCO-IRIS Joint Workshop, Stevenson, Washington, 8–11 June.

Blewitt, G., J. W. Bell, W. C. Hammond, C. Kreemer, H.-P. Plag, and C. M. dePolo (2008), GPS and InSAR monitoring of the Mogul Swarm: Evidence for mainly aseismic fault creep, with implications for seismic hazard, *Eos Trans. AGU*, *89*(53), Fall Meet. Suppl., Abstract S53C–03.

Blewitt, G., W. C. Hammond, and C. Kreemer (2009), Geodetic constraints on contemporary deformation in the northern Walker Lane: 1. Semipermanent GPS strategy, in *Late Cenozoic Structure and Evolution of the Great Basin–Sierra Nevada Transition*, edited by J. S. Oldow and P. Cashman, *Spec. Pap. Geol. Soc. Am.*, *447*, 1–15, doi:10.1130/2009.2447(01).

Briggs, R. W., and S. G. Wesnousky (2004), Late Pleistocene fault slip rate, earthquake recurrence, and recency of slip along the Pyramid Lake fault zone, northern Walker Lane, United States, *J. Geophys. Res.*, *109*, B08402, doi:10.1029/2003JB002717.

Cashman, P., and S. A. Fontaine (2000), Strain partitioning in the northern Walker Lane, western Nevada and northeastern California, *Tectonophysics*, *326*, 111–130, doi:10.1016/S0040-1951(00)00149-9.

Cashman, P., J. H. Trexler Jr., T. W. Muntean, J. E. Faulds, J. N. Louie, and G. Oppliger (2009), Neogene tectonic evolution of the Sierra Nevada-Basin and Range transition zone at the latitude of Carson City, in *Late Cenozoic Structure and Evolution of the Great Basin–Sierra Nevada Transition*, edited by J. S. Oldow and P. Cashman, *Spec. Pap. Geol. Soc. Am.*, *447*, 171–188.

DeMets, C., R. G. Gordon, D. F. Argus, and S. Stein (1994), Effect of recent revisions to the geomagnetic reversal time-scale on estimates of current plate motions, *Geophys. Res. Lett.*, *21*, 2191–2194, doi:10.1029/94GL02118.

Dixon, T. H., M. Miller, F. Farina, H. Wang, and D. Johnson (2000), Present-day motion of the Sierra Nevada block and some tectonic implications for the Basin and Range province, North American Cordillera, *Tectonics*, *19*, 1–24, doi:10.1029/1998TC001088.

Dixon, T. H., E. Norabuena, and L. Hotaling (2003), Paleoseismology and Global Positioning System: Earthquake-cycle effects and geodetic versus geologic fault slip rates in the Eastern California Shear Zone, *Geology*, *31*, 55–58, doi:10.1130/0091-7613(2003)031<0055:PAGPSE>2.0.CO;2.

Dokka, R. K., and C. J. Travis (1990), Role of the Eastern California Shear Zone in accommodating Pacific-North-American plate motion, *Geophys. Res. Lett.*, *17*, 1323–1326, doi:10.1029/GL017i009p01323.

Doser, D. I. (1988), Source parameters of earthquakes in the Nevada seismic zone, 1915–1943, *J. Geophys. Res.*, *93*, 15,001–15,015.

Doser, D. I., and R. B. Smith (1989), An assessment of source parameters of earthquakes in the Cordillera of the Western United-States, *Bull. Seismol. Soc. Am.*, *79*, 1383–1409.

Faulds, J. E., and C. D. Henry (2008), Tectonic influences on the spatial and temporal evolution of the Walker Lane: An incipient transform fault along the evolving Pacific–North American plate boundary, in *Ores and Orogenesis: Circum-Pacific Tectonics, Geologic Evolution, and Ore Deposits*, edited by J. E. Spencer and S. R. Titley, pp. 437–470, Ariz. Geol. Soc., Tucson.

Faulds, J. E., and M. E. Perkins (2007), Evidence for dextral shear along the western margin of the Carson Sink: The missing link between the central and northern Walker Lane, western Nevada, *Geol. Soc. Am. Abstr. Programs*, *39*(4), 15.

Faulds, J. E., and A. R. Ramelli (2005), Preliminary geologic map of the Fernley East Quadrangle, Lyon and Washoe Counties, Nevada, *Open File Rep. 05–9*, scale 1:24,000, Nev. Bur. of Mines and Geol., Reno.

Faulds, J. E., M. Coolbaugh, G. Blewitt, and C. D. Henry (2004), Why is Nevada in hot water? Structural controls and tectonic model of geothermal systems in the northwestern Great Basin, *Trans. Geotherm. Res. Counc.*, *28*, 649–654.

Faulds, J. E., C. D. Henry, and N. H. Hinz (2005), Kinematics of the northern Walker Lane: An incipient transform fault along the Pacific-North American plate boundary, *Geology*, *33*, 505–508, doi:10.1130/G21274.1.

Freed, A. M., R. Bürgmann, and T. Herring (2007), Far-reaching transient motions after Mojave earthquakes require broad mantle flow beneath a strong crust, *Geophys. Res. Lett.*, *34*, L19302, doi:10.1029/2007GL030959.

Freund, L. B., and D. M. Barnett (1976), A two-dimensional analysis of surface deformation due to dip-slip faulting, *Bull. Seismol. Soc. Am.*, *66*, 667–675.

Goter, S. K., D. H. Oppenheimer, J. J. Mori, M. K. Savage, and R. P. Masse (1994), Earthquakes in California and Nevada, *U.S. Geol. Surv. Open File Rep.*, *94–647*.

Gourmelen, N., and F. Amelung (2005), Post-seismic deformation in the Central Nevada Seismic Belt detected by InSAR: Implications for Basin and Range dynamics, *Science*, *310*, 1473–1476, doi:10.1126/science.1119798.

Hammond, W. C., and W. Thatcher (2004), Contemporary tectonic deformation of the Basin and Range Province, western United States: 10 years of observation with the Global Positioning System, *J. Geophys. Res.*, *109*, B08403, doi:10.1029/2003JB002746.

Hammond, W. C., and W. Thatcher (2007), Crustal deformation across the Sierra Nevada, northern Walker Lane, Basin and Range transition, western United States measured with GPS, 2000–2004, *J. Geophys. Res.*, *112*, B05411, doi:10.1029/2006JB004625.

Hammond, W. C., C. Kreemer, and G. Blewitt (2009), Geodetic constraints on contemporary deformation in the northern Walker Lane: 3. Postseismic relaxation in the Central Nevada Seismic Belt, in *Late Cenozoic Structure and Evolution of the Great Basin–Sierra Nevada Transition*, edited by J. S. Oldow and P. Cashman, *Spec. Pap. Geol. Soc. Am.*, *447*, 33–54, doi:10.1130/2009.2447(03).

Hammond, W. C., C. Kreemer, G. Blewitt, and H.-P. Plag (2010), Effect of viscoelastic postseismic relaxation on estimates of interseismic crustal strain accumulation at Yucca Mountain, Nevada, *Geophys. Res. Lett.*, *37*, L06307, doi:10.1029/2010GL042795.

Hammond, W. C., G. Blewitt, C. Kreemer, J. R. Murray-Moraleda, and J. Svarc (2011), GPS constraints on crustal deformation before and during the 21 February 2008 Wells, Nevada M 6.0 earthquake, *Spec. Publ. Nev. Bur. Mines Geol.*, *36*, 181–195.

Hetland, E. A., and B. H. Hager (2003), Postseismic relaxation across the Central Nevada Seismic Belt, *J. Geophys. Res.*, *108*(B8), 2394, doi:10.1029/2002JB002257.

Hinz, N. H., J. E. Faulds, and C. D. Henry (2009), Tertiary volcanic stratigraphy and paleotopography of the Diamond and Fort Sage mountains: Constraining slip along the Honey Lake fault zone in the northern Walker Lane, northeastern California and western Nevada, in *Late Cenozoic Structure and Evolution of the Great Basin–Sierra Nevada Transition*, edited by J. S. Oldow and P. Cashman, *Geol. Soc. Am. Spec. Pap.*, *447*, 101–131, doi:10.1130/2009.2447(07).

Howell, D. G. (1976), A model to accommodate 1000 kilometres of right-slip, Neogene displacement in the southern California area, in *Aspects of the Geologic History of the California Continental Borderland Pacific Section*, vol. 24, edited by D. G. Howell, pp. 530–540, Am. Assoc. of Pet. Geol., Tulsa, Okla.

Ichinose, G. A., J. G. Anderson, K. D. Smith, and Y. Zeng (2003), Source parameters of eastern California and western Nevada earthquakes from regional moment tensor inversion, *Bull. Seismol. Soc. Am.*, *93*, 61–84, doi:10.1785/0120020063.

Kent, G. M., et al. (2005), 60 k.y. record of extension across the western boundary of the Basin and Range province: Estimate of slip rates from offset shoreline terraces and a catastrophic slide beneath Lake Tahoe, *Geology*, *33*, 356–368, doi:10.1130/G21230.1.

Kreemer, C., G. Blewitt, and W. C. Hammond (2009), Geodetic constraints on contemporary deformation in the northern Walker Lane: 2. Velocity and tensor strain rate analysis, in *Late Cenozoic Structure and Evolution of the Great Basin–Sierra Nevada Transition*, edited by J. S. Oldow and P. Cashman, *Spec. Pap. Geol. Soc. Am.*, *447*, p. 33–54, doi:10.1130/2009.2447(03).

Lamb, S. H. (1994), Behavior of the brittle crust in wide plate boundary zones, *J. Geophys. Res.*, *99*, 4457–4483, doi:10.1029/93JB02574.

Langbein, J., and H. Johnson (1997), Correlated errors in geodetic time series: Implications for time-dependent deformation, *J. Geophys. Res.*, *102*, 591–603, doi:10.1029/96JB02945.

Machette, M. N., K. M. Haller, K. Okumura, S. Ruleman, S. Debray, and S. Mahan (2002), Paleoseismology of the Clan Alpine Fault, west-central Nevada, *Geol. Soc. Am. Abstr. Programs*, *34*(4), 3.

Mao, A. C., G. A. Harrision, and T. H. Dixon (1999), Noise in GPS coordinate time series, *J. Geophys. Res.*, *104*, 2797–2816, doi:10.1029/1998JB900033.

Matsu'ura, M., D. D. Jackson, and A. Cheng (1986), Dislocation model for aseismic crustal deformation at Hollister, California, *J. Geophys. Res.*, *91*, 12,661–12,674, doi:10.1029/JB091iB12p12661.

McCaffrey, R. (2002), Crustal block rotations and plate coupling, in *Plate Boundary Zones*, *Geodyn. Ser.*, vol. 30, edited by S. A. Stein and J. Freymueller, pp. 101–122, AGU, Washington, D. C.

McCaffrey, R. (2005), Block kinematics of the Pacific-North America plate boundary in the southwestern United States from inversion of GPS, seismological and geologic data, *J. Geophys. Res.*, *110*, B07401, doi:10.1029/2004JB003307.

McCaffrey, R., A. I. Qamar, R. W. King, R. Wells, G. Khazaradze, C. A. Williams, C. W. Stevens, J. J. Vollick, and P. C. Zwick (2007), Fault locking, block rotation and crustal deformation in the Pacific Northwest, *Geophys. J. Int.*, *169*, 1315–1340, doi:10.1111/j.1365-246X.2007.03371.x.

McClusky, S. C., S. C. Bjornstad, B. H. Hager, R. W. King, B. J. Meade, M. Miller, F. C. Monastero, and B. J. Souter (2001), Present day kinematics of the Eastern California Shear Zone from a geodetically constrained block model, *Geophys. Res. Lett.*, *28*, 3369–3372, doi:10.1029/2001GL013091.

Meade, B. J., and B. H. Hager (2005), Block models of crustal motion in southern California constrained by GPS measurements, *J. Geophys. Res.*, *110*, B03403, doi:10.1029/2004JB003209.

Murray, J. R., P. Segall, P. Cervelli, W. H. Prescott, and J. L. Svarc (2001), Inversion of GPS data for spatially variable slip-rate on the San Andreas Fault near Parkfield, CA, *Geophys. Res. Lett.*, *28*, 359–362, doi:10.1029/2000GL011933.

Nur, A., and G. Mavko (1974), Postseismic viscoelastic rebound, *Science*, *183*, 204–206, doi:10.1126/science.183.4121.204.

Okada, Y. (1985), Surface deformation due to shear and tensile faults in a half-space, *Bull. Seismol. Soc. Am.*, *75*, 1135–1154.

Oldow, J. S. (2003), Active transtensional boundary zone between the western Great Basin and Sierra Nevada block, western U.S. Cordillera, *Geology*, *31*, 1033–1036, doi:10.1130/G19838.1.

Oldow, J. S., C. L. V. Aiken, J. L. Hare, J. F. Ferguson, and R. F. Hardyman (2001), Active displacement transfer and differential block motion within the central Walker Lane, western Great Basin, *Geology*, *29*, 19–22, doi:10.1130/0091-7613(2001)029<0019:ADTADB>2.0.CO;2.

Pancha, A., J. G. Anderson, and C. Kreemer (2006), Comparison of seismic and geodetic scalar moment rates across the Basin and Range province, *Bull. Seismol. Soc. Am.*, *96*, 11–32, doi:10.1785/0120040166.

Parsons, T. (2002), Nearly frictionless faulting by unclamping in long-term interaction models, *Geology*, *30*, 1063–1066, doi:10.1130/0091-7613(2002)030<1063:NFFBUI>2.0.CO;2.

Pollitz, F. F. (1997), Gravitational-viscoelastic postseismic relaxation on a layered spherical Earth, *J. Geophys. Res.*, *102*, 17,921–17,941.

Pollitz, F. F., G. Peltzer, and R. Burgmann (2000), Mobility of continental mantle: Evidence from postseismic geodetic observation following the 1992 Landers earthquake, *J. Geophys. Res.*, *105*, 8035–8054, doi:10.1029/1999JB900380.

Pollitz, F. F., P. McCrory, J. Svarc, and J. Murray (2008), Dislocation models of interseismic deformation in the western United States, *J. Geophys. Res.*, *113*, B04413, doi:10.1029/2007JB005174.

Prawirodirdjo, L., et al. (1997), Geodetic observations of interseismic strain segmentation at the Sumatra subduction zone, *Geophys. Res. Lett.*, *24*, 2601–2604, doi:10.1029/97GL52691.

Ramelli, A. R., J. W. Bell, C. M. dePolo, and J. C. Yount (1999), Large-magnitude, late Holocene earthquakes on the Genoa Fault, west-central Nevada and eastern California, *Bull. Seismol. Soc. Am.*, *89*, 1458–1472.

Reilinger, R., et al. (2006), GPS constraints on continental deformation in the Africa-Arabia-Eurasia continental collision zone and implications for the dynamics of plate interactions, *J. Geophys. Res.*, *111*, B05411, doi:10.1029/2005JB004051.

Savage, J. C. (1983), A dislocation model of strain accumulation and release at a subduction zone, *J. Geophys. Res.*, *88*, 4984-4996.

Savage, J. C., and R. O. Burford (1973), Geodetic determination of relative plate motion in central California, *J. Geophys. Res.*, *78*, 832–845, doi:10.1029/JB078i005p00832.

Savage, J. C., and W. H. Prescott (1978), Asthenosphere readjustment and the earthquake cycle, *J. Geophys. Res.*, *83*, 3369–3376, doi:10.1029/JB083iB07p03369.

Savage, J. C., W. Gan, and J. L. Svarc (2001), Strain accumulation and rotation in the eastern California shear zone, *J. Geophys. Res.*, *106*, 21,995–22,007.

Sawyer, T. L., R. W. Briggs, and A. R. Ramelli (2005), Late Quaternary activity of the Southern Mohawk Valley fault zone, northeastern California, *Seismol. Res. Lett.*, *76*, 248.

Schweickert, R. A., M. M. Lahren, R. Karlin, J. Howle, and K. D. Smith (2000), Lake Tahoe active faults, landslides, and tsunamis, in *Great Basin and Sierra Nevada: Field Guide 2*, edited by D. R. Lageson et al., pp. 1–21, Geol. Soc. of Am., Boulder, Colo., doi:10.1130/0-8137-0002-7.1.

Schweickert, R. A., M. M. Lahren, K. D. Smith, J. Howle, and G. Ichinose (2004), Transtensional deformation in the Lake Tahoe region, California and Nevada, USA, *Tectonophysics*, *392*, 303–323, doi:10.1016/j.tecto.2004.04.019.

Segall, P. (2002), Integrating geologic and geodetic estimates of slip rate on the San Andreas fault system, *Int. Geol. Rev.*, *44*(1), 62–82, doi:10.2747/0020-6814.44.1.62.

Stewart, J. H. (1988), Tectonics of the Walker Lane belt, western Great Basin: Mesozoic and Cenozoic deformation in a zone of shear, in *Metamorphism and Crustal Evolution of the Western United States*, edited by W. G. Ernst, pp. 681–713, Prentice Hall, Englewood Cliffs, N. J.

Surpless, B. (2008), Modern strain localization in the central Walker Lane, western United States: Implications for the evolution of intraplate deformation in transtensional settings, *Tectonophysics*, *457*, 239–253, doi:10.1016/j.tecto.2008.07.001.

Svarc, J. L., J. C. Savage, W. H. Prescott, and A. R. Ramelli (2002), Strain accumulation and rotation in western Nevada, 1993–2000, *J. Geophys. Res.*, *107*(B5), 2090, doi:10.1029/2001JB000579.

Thatcher, W. (2009), How the continents deform: The evidence from tectonic geodesy, *Annu. Rev. Earth Planet. Sci.*, *37*, 237–262, doi:10.1146/annurev.earth.031208.100035.

Thatcher, W., and D. P. Hill (1991), Fault orientations in extensional and conjugate strike-slip environments and their implications, *Geology*, *19*, 1116–1120, doi:10.1130/0091-7613(1991)019<1116:FOIEAC>2.3.CO;2.

Thatcher, W., G. R. Foulger, B. R. Julian, J. L. Svarc, E. Quilty, and G. W. Bawden (1999), Present-day deformation across the Basin and Range province, western United States, *Science*, *283*, 1714–1718, doi:10.1126/science.283.5408.1714.

Turner, R., R. Koehler, R. W. Briggs, and S. G. Wesnousky (2008), Reevauaton of the fault slip rate and paleoseismic history of the Honey Lake fault zone, northeastern California, *Bull. Seismol. Soc. Am.*, *98*, 1730–1736, doi:10.1785/0120070090.

Unruh, J. R., J. Humphrey, and A. Barron (2003), Transtensional model for the Sierra Nevada frontal fault system, eastern California, *Geology*, *31*, 327–330, doi:10.1130/0091-7613(2003)031<0327:TMFTSN>2.0.CO;2.

U.S. Geological Survey and Nevada Bureau of Mines and Geology (2006), Quaternary fault and fold database for the United States, accessed September 2007 to November 2010, http//earthquakes.usgs.gov/regional/qfaults/, Reno, Nev.

Wallace, K., G. H. Yin, and R. Bilham (2004), Inescapable slow slip on the Altyn Tagh fault, *Geophys. Res. Lett.*, *31*, L09613, doi:10.1029/2004GL019724.

Wdowinski, S., Y. Bock, J. Zhang, P. Fang, and J. Genrich (1997), Southern California Permanent GPS Geodetic Array: Spatial filtering of daily positions for estimating coseismic and postseismic displacements induced by the 1992 Landers earthquake, *J. Geophys. Res.*, *102*, 18,057–18,070, doi:10.1029/97JB01378.

Wernicke, B. P., and K. J. Snow (1998), Cenozoic tectonism in the central Basin and Range: Motion of the Sierran-Great Valley block, *Int. Geol. Rev.*, *40*, 403–410, doi:10.1080/00206819809465217.

Wernicke, B. P., A. M. Friedrich, N. A. Niemi, R. A. Bennett, and J. L. Davis (2000), Dynamics of plate boundary fault systems from Basin and Range Geodetic Network (BARGEN) and geologic data, *GSA Today*, *10*, 1–7.

Wesnousky, S. G. (2005a), Active faulting in the Walker Lane, *Tectonics*, *24*, TC3009, doi:10.1029/2004TC001645.

Wesnousky, S. G. (2005b), The San Andreas and Walker Lane fault systems, western North America: Transpression, transtension, cumulative slip and the structural evolution of a major transform plate boundary, *J. Struct. Geol.*, *27*, 1505–1512, doi:10.1016/j.jsg.2005.01.015.

Wesnousky, S. G., A. D. Baron, R. W. Briggs, J. S. Caskey, S. J. Kumar, and L. Owen (2005), Paleoseismic transect across the northern Great Basin, *J. Geophys. Res.*, *110*, B05408, doi:10.1029/2004JB003283.

Williams, S. P. D. (2003), The effect of coloured noise on the uncertainties of rates estimated from geodetic time series, *J. Geod.*, *76*, 483–494, doi:10.1007/s00190-002-0283-4.

Williams, S. P. D., Y. Bock, P. Fang, P. Jamason, R. M. Nikolaidis, and L. Prawirodirdjo (2004), Error analysis of continuous GPS position time series, *J. Geophys. Res.*, *109*, B03412, doi:10.1029/2003JB002741.

Wills, C. J., and G. Borchardt (1993), Holocene slip rate and earthquake recurrence on the Honey Lake fault zone, northeastern California, *Geology*, *21*, 853–856, doi:10.1130/0091-7613(1993)021<0853:HSRAER>2.3.CO;2.

Zumberge, J. F., M. B. Heflin, D. C. Jefferson, M. M. Watkins, and F. H. Webb (1997), Precise point positioning for the efficient and robust analysis of GPS data from large networks, *J. Geophys. Res.*, *102*, 5005–5017, doi:10.1029/96JB03860.

G. Blewitt, W. C. Hammond, and C. Kreemer, Nevada Geodetic Laboratory, Nevada Bureau of Mines and Geology and Nevada Seismological Laboratory, University of Nevada, Reno, NV 89557, USA. (whammond@unr.edu)